https://doi.org/10.1016/j.cemconres.2022.107034

Effect of seawater on the morphology, structure, and properties of synthetic ettringite

Yamei Cai [a], Yong Tao [a,b,*], Dongxing Xuan [a], Yanjie Sun [a], Chi Sun Poon [a,*]

[a] Department of Civil and Environmental Engineering, The Hong Kong Polytechnic University, Hong Kong

[b] State Key Laboratory of Silicate Materials for Architectures, Wuhan University of Technology. Wuhan, Hubei 430070, China

*Corresponding author. Email addresses: yong.tao@polyu.edu.hk (Yong Tao) and cecspoon@polyu.edu.hk (Prof. Chi Sun Poon)

Abstract: This work investigated the influence of seawater on the growth rate, morphology, and properties of ettringite (AFt). The results showed that, in the absence of calcium hydroxide (CH), a part of the Mg ions in seawater preferentially formed Mg-Al layered double hydroxide containing Cl^- (Mg-Al-Cl LDH), which could accelerate the subsequent precipitation of AFt in seawater. However, in the presence of CH, some of the Mg ions in seawater formed brucite, and there was no significant acceleration for the precipitation of AFt in the seawater-CH solution, compared with the AFt formed in seawater without CH. Besides, in both cases with and without CH, some Mg ions in seawater could enter the sites of Ca in the AFt structure, leading to an unstable structure. This would cause a relatively lower packing density compared with the corresponding AFt samples synthesized in deionized (DI) water, further leading to a relatively lower mechanical property. When the Mg ions were excluded from seawater, the AFt samples synthesized seemed to have a relatively higher packing density compared with the corresponding AFt formed in DI water, resulting in a relatively higher mechanical property. This finding could lead to a better understanding of the degradation of the micromechanical properties of AFt in seawater-mixed cementitious materials caused by the Mg ions.

Keywords: Seawater; Ettringite; Hydration; Mechanical property; Atomistic simulations

1. Introduction

In concrete production, the possible use of seawater as the mixing water to replace freshwater has attracted increasing attention, especially for concrete produced with no steel corrosion issues, such as reinforcement-free concrete and non-metallic reinforcement concrete [1-3]. Previous studies showed that the incorporation of seawater accelerated the hydration of cementitious materials [4-7]. It was reported that, compared with freshwater, the ions present in seawater can increase the ionic strength of the pore solution and consequently decrease the activity coefficient of solute ions, which would further increase the concentration of ions, *e.g.*, Ca species [8, 9]. Thus, the higher ionic concentration would accelerate the dissolution of tricalcium silicate and tricalcium aluminate in cement [8, 9], which would further increase the nucleation rate of hydration products [10].

As an important hydration product of the aluminate phase, ettringite plays a crucial role in the control of the setting before the hardening of cement. It also affects the short-term strength development of cementitious materials [11, 12], especially for rapid hardening cements, such as calcium sulfoaluminate cement [13-15] and calcium aluminate cement incorporated with calcium sulphates [16]. Nevertheless, the formation of ettringite in matured/hardened cement and concrete can lead to strength degradation due to volume expansions, such as in cases of sulphate attack [17, 18] and delayed ettringite formation [19].

As for the effect of seawater on the formation of ettringite in cement, the previous study mainly revealed the accelerating influence of seawater, which was mainly attributed to a greater supersaturation of ettringite in seawater due to the larger dissolution driving force of tricalcium aluminate (C_3A) and the higher solubility of gypsum in seawater [9]. However, research on the

influence of various ions present in seawater on the morphology, structure, and properties of ettringite is scarce. Cody et al. [20] studied the nucleation, growth, and morphology of ettringite in the presence of over 300 organic/inorganic chemical additives, including water reducers, set retarders, accelerators, air-entraining admixtures, *etc*. The organic chemical additives were grouped according to the types of organic functional groups, and the general trends of these organic chemicals affecting the ettringite nucleation and growth were summarised [20]. As for ionic species present in the inorganic additives, it was found that single-valent ions had little effect on the formation of the synthesized ettringite, but the presence of $MgCl_2$ made the ettringite crystals shorter and thinner [20]. However, the effects of multi-ions, such as in the case of seawater, on the growth and properties of ettringite are unclear. Besides, the ettringite studied in Ref. [20] was produced by using aluminium sulphate solution ($Al_2(SO_4)_3 \cdot 18H_2O$) and calcium hydroxide ($Ca(OH)_2$), which was quite different from the formation process of ettringite in cement and concrete environments.

The objective of this work is to fill this research gap and try to further understand the influence of ions in seawater on the structure and properties of ettringite formed in seawater-mixed cementitious materials.

In this work, ettringite was synthesized using C_3A and gypsum in deionized water (DI) and simulated seawater (SW). Additionally, considering the presence of portlandite during the formation of ettringite in hydrated Portland cement, the ettringite was also synthesized in DI-saturated calcium hydroxide (DI-sat. CH) and SW-sat.CH solutions. Then, the properties of the synthetic different ettringite samples were characterized by using X-ray diffraction (XRD), scanning electron microscopy (SEM), nanoindentation, BET, pH meter, thermogravimetric and differential thermal analysis (TG/DTA), and Fourier-transform infrared spectroscopy (FTIR). Furthermore, the first-principles calculations and molecular dynamics simulations were applied

to theoretically evaluate the possible incorporation of Mg ions in the ettringite structure and its effects on the stability and elastic properties of the produced ettringite crystals.

2. Materials and experimental methods

2.1. Raw materials

A similar cubic C_3A source provided by a commercial laboratory as shown in our previous work [21] was used in this work. The X-ray diffraction pattern (XRD) and particle size distribution (PSD) of this new batch of C_3A were displayed in Figs. S.1 and S.2 in the supplementary material. The XRD result shows that the purity of C_3A was about 98%, besides free lime and mayenite ($C_{12}A_7$) accounted for 0.45 % and 1.6 %, respectively. The PSD data indicates that the median particle size of C_3A was 7.68 μm. Besides, the same gypsum with a median particle diameter of 22.4 μm as presented in our previous study [9] was also used in this work.

Based on the procedure in the ASTM D 1141-98 [22], the simulated seawater (SW) was prepared, and its pH value was about 8.1. The chemical compositions of this SW were 24.53 g/L NaCl, 5.20 g/L $MgCl_2$, 4.09 g/L Na_2SO_4, 1.16 g/L $CaCl_2$, 0.695 g/L KCl, 0.201 g/L $NaHCO_3$, 0.101 g/L KBr, 0.027 g/L H_3BO_3, 0.025 g/L $SrCl_2$, and 0.003 g/L NaF, and the ionic concentrations of SW had been shown in Ref. [21].

2.2. Synthesis procedure of ettringite

Ettringite (AFt) was synthesized at 22 ± 1 °C using C_3A and gypsum. Two types of solution environments were selected, *i.e.*, in the absence of calcium hydroxide (CH) and in the saturated CH (sat.CH) environment. In the solution environment without CH, DI water, SW and seawater excluding $MgCl_2$ (SW-no $MgCl_2$) were used to synthesize the different AFt samples. In the sat.CH environment, two AFt samples were formed in the pre-prepared DI-sat.CH solution and

seawater-sat.CH solution (SW-sat.CH). But, in the process of preparing SW-sat.CH solution, the Mg ions in seawater would combine with OH^- from CH forming brucite ($Mg(OH)_2$), which was then removed by filtering. In contrast, an appropriate amount of CH was added to the C_3A-gypsum solid, and then seawater was directly added to this mixture to prepare the third AFt specimen (SW-CH-AFt). In this process, the reaction products associated with Mg were also included in this reaction system. The evolution of the pH value of seawater with the dosage of CH is shown in Fig. 1, and a 6.5 g CH per liter of seawater was used to synthesize the SW-CH-AFt sample.

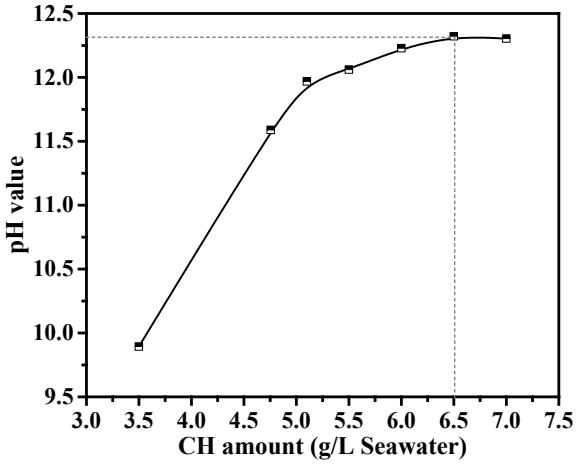

Fig. 1. Development of pH value of seawater with the increase of calcium hydroxide.

The specific synthetic process is as follows. According to the stoichiometric ratio, a 1:3 molar mixture of C_3A and gypsum was used to synthesize the AFt samples in DI water or DI-sat.CH solution. Besides, considering that seawater contains 2.8 g/L SO_4^{2-}, a 1: 2.6 molar mixture of C_3A and gypsum was used to synthesize the AFt samples in different seawater solutions. A certain proportion of C_3A and gypsum as mentioned above were first mixed thoroughly, and the detailed mixing process had been given in Ref. [9]. Then measured amounts of the C_3A-gypsum mixture were placed in 50 mL centrifugal tubes. After that, the above different solutions with a liquid-to-solid (l/s) ratio of 20 were added into these tubes.

Next, lids were inserted before these tubes were vigorously agitated using a vortex apparatus for 2 min and then rotated at 50 rpm in an end-over-end rotator for at least 28 d. Finally, filtrates were obtained through 0.45 μm cellulose membrane filters after centrifugation at 10,000 rpm for 5 min. The pH values of these filtrates were immediately recorded as described in Section 2.3.5. Isopropanol was then immediately poured into the solid residues. After vigorous shaking for 2 h, the solid residues were obtained again by centrifugation and dried in a vacuum oven at 40 ^{o}C for 2 d. Then, the samples were placed in a vacuum desiccator containing silica gel until further use.

2.3. Experimental techniques

2.3.1. Mineralogy analysis of the synthetic AFt samples

The formation amount of AFt for the synthetic AFt samples at different reaction times was characterized using a Rigaku SmartLab X-ray diffractometer (XRD) operated at 45 kV and 200 mA with CuKα radiation (λ=1.54 Å). A quantitative X-ray diffraction (QXRD) technique adopting an internal standard method of 10 wt.% corundum was used. The scanned parameters of samples were in the 5 - 60 ^{o} 2θ range, with an increment of 0.02 ^{o} and at a speed of 2.5 ^{o}/min. The details of Rietveld refinement analysis of the XRD pattern, such as the analysis software and optimized parameters, had been given in Ref. [9]. In addition, qualitative X-ray diffraction was also applied. The scan speed used was 5 ^{o}/min, and other test parameters were similar to that of the quantitative test as described above.

Furthermore, using a Scherrer calculator in EVA software, the average crystallite sizes of the different synthetic AFt crystals were calculated based on the positions and half-widths of (100), (110), and (114) peaks.

2.3.2. Morphology analysis of the synthetic AFt

The morphology of synthetic AFt was observed by a field emission scanning electron microscope (FESEM, TESCAN MAIA3). This test was carried out in a depth scan mode with an accelerating voltage of 5 kV and a working distance of ~ 4 mm. The synthetic AFt suspension prepared as described in Section 2.2 was diluted by 50 using Milli-Q water to reduce the possible stacking of AFt crystals. Then the diluted liquid was deposited onto an ultra-flat polished silicon chip (8 mm × 8 mm) that was stuck on a microscopy stub using an adhesive carbon tape. After that, this sample was gold-coated by using a CRESSINGTON sputter coater before observation.

The length of AFt in the captured pictures by SEM instrument was measured using ImageJ software. At least 200 data points were counted for each AFt sample.

2.3.3. Micromechanical analysis of the synthetic AFt

The nanoindentation technique was conducted to characterize the micromechanical properties of the synthetic AFt samples using a Nano-indenter (Hysitron TI Premier, Bruker) equipped with Scanning Probe Microscopy (SPM). As for the sample preparation, at first, the powder collected in Section 2.2 was pressed into disc-shaped specimens of about 13 mm in diameter by about 4 mm in thickness at a pressure of 30 MPa for 30 s. Then these samples were embedded in epoxy. After hardening at 30 ^{o}C, these samples were ground and polished successively with 600 and 1200 grit SiC sanding paper, followed by polishing cloths with successively finer polishing agents (9 μm, 3 μm, and 0.05 μm). In the above process, the samples were cleaned between each step using ethanol in an ultrasonic bath. Besides, ethanol instead of water where needed was used as a lubricant.

After polishing, the surface roughness of the samples was monitored using SPM scanning on a 50 μm × 50 μm area in order to check the polishing quality of the sample surface [23]. The final root-mean-squared (RMS) roughness was about 45 nm as shown in Fig. 2.

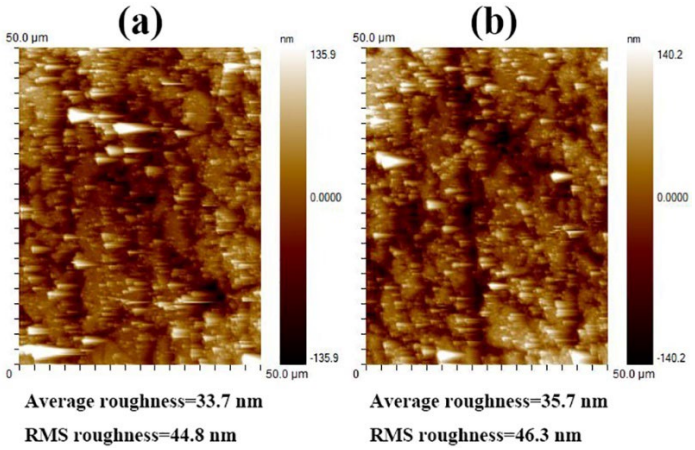

Fig. 2. SPM images of the polished sample surface. (a) and (b) are two different regions of a sample.

After inspecting the sample surface, the micro-mechanical property of the synthetic AFt samples was assessed. For each sample, four different regions were selected. The unreacted gypsum and C_3A could be roughly identified as described in Fig. S.5 in the supplementary material, which was not chosen in the test regions. For each region, a 10 × 10 grid with a grid spacing of 10 µm was applied. Thus, 400 points were collected for each sample. In addition, the loading function adopted in this test had been described in Ref. [24].

From this test, two micro-mechanical parameters, *i.e.*, reduced modulus (E_r) and hardness (H), can be obtained. The elastic modulus (E_p) of the synthetic AFt can be derived from the following equation (2-1):

$$\frac{1}{E_r}=\frac{1-\nu^2}{E_p}+\frac{1-\nu_i^2}{E_i} \quad (2\text{-}1)$$

Where E_r is the reduced modulus of tested samples. E_i and ν_i are the parameters of the indenter tip (E_i=1140 GPa and ν_i=0.07 for diamond tip [25]). E_p and ν denote the elastic modulus and Poisson's ratio of the tested samples. A Poisson's ratio of 0.34 for the AFt crystal was used in this study [26-28].

Additionally, the packing density ('one minus porosity') of the synthetic different AFt samples was calculated based on the obtained nanoindentation data, *i.e.*, a series of indentation

modulus and hardness data points. The calculation method had been described in detail by Ulm et al [29].

2.3.4. Elemental analysis

After the nanoindentation test, the polished samples prepared in Section 2.3.3 were used to identify the elemental composition of the synthetic AFt by using a scanning electron microscope (SEM, TESCAN VEGA3) equipped with an energy dispersive X-ray spectrometer (EDS). At first, the polished sample surface was carbon coated by using an SPI Module™ Carbon Coater. Then, a backscattered electron (BSE) mode if imaging was used at an accelerating voltage of 20 kV, a working distance of ~ 13 mm and a magnification of × 4000. During this measurement, at least 10 different regions across the sample were chosen, and unreacted gypsum and C_3A were not selected as described in Fig. S.6 and Table S.3 of the supplementary material. In each region, 10 points with a spacing of at least 20 μm were measured. Therefore, the total EDS points measured were at least 100. Based on the EDS data, the atomic percentages of various elements were used to characterize the elemental composition of the synthetic AFt samples.

2.3.5. pH value measurement

The pH evolution in the reaction solution of the synthetic AFt samples was in-situ monitored using a digital display pH meter with a precision of 0.001 (SevenExcellence, METTLER TOLEDO). Before measurement, the commercial buffers at pH of 4.01, 7.00, 9.21, and 10.01 were used to calibrate the pH meter.

At first, 50 g of different liquids, including DI, SW, *etc*., was poured into a 50 mL glass beaker. Then, a pH probe was immersed into this solution to continuously record the pH value. During the test, the solution was stirred with a magnetic stirrer with a stirring speed of 300 rpm.

Then, a 2.5 g mixture of C_3A and gypsum (l/s=20) as prepared in Section 2.2 was added to this beaker. Finally, this beaker was sealed using Parafilm to prevent carbonation, and the in-situ pH test was continuously carried out for 2 d.

Besides, the pH value of the filtrates at 28 d of the synthetic AFt samples collected in Section 2.2 was measured immediately.

2.3.6. Pore structure analysis of the synthetic AFt samples

The pore structure of the AFt samples synthesized in different solutions was characterized by a BET multi-point nitrogen physisorption apparatus (Micromeritics ASAP 2020 plus). Before measurement, the sample was degassed at 40 ^{o}C under N_2 flow for 16 h. The nitrogen adsorption was carried out using a twelve-point isotherm in a relative pressure P/P_0 range of 0.06 to 0.28 at -196 ^{o}C. Based on the Barret-Joyner-Halenda (BJH) method [30], the pore size distribution was computed using the adsorption isotherm, considering that the tortuosity and pore shape were less likely to affect the adsorption curves than the desorption curves [31].

2.3.7. Thermogravimetric and differential thermal analysis

Thermogravimetric and differential thermal analysis (TG/DTA) were carried out for the different synthetic AFt samples. 9 ± 0.2 mg of each AFt sample was placed in alumina crucibles. Then, these samples were heated in an Argon atmosphere from 30 ^{o}C to 800 ^{o}C at a rate of 10 ^{o}C/min using a TG/DTA 8121 analyser (Rigaku, Japan). The brucite and carbonates contents were calculated using the tangential method [32, 33], and the results were rescaled after considering the free water bound into the hydration products [33].

2.3.8. Fourier-transform infrared spectroscopy

A Fourier-transform infrared (FT-IR) spectrometer was applied to monitor reaction phases using a PerkinElmer UATR Two equipped with diamond tipped ATR stage (Spectrum Two, PerkinElmer). The background and sample spectra were scanned in the wavenumber range from 4000 cm^{-1} to 400 cm^{-1} with a resolution of 4 cm^{-1}. Each spectrum was scanned 16 times to ensure accuracy.

2.4. Atomistic simulations

In this study, we find that the Mg ions in seawater have significant influences on the micromechanical properties of AFt. Previous studies reported by Cody et al. [20] and Albino et al. [34] proposed that the Ca ions in the crystal lattice of AFt were possibly substituted by Mg ions. Therefore, we conducted additional atomistic simulations to provide atomic-scale insights into the possibility of Mg-doped AFt crystals, and the effects of Mg incorporated into the AFt structure were further elucidated.

2.4.1 Defect formation energy calculations

While elemental analysis can depict the distribution of Mg ions in the hydration product mixture, more direct methods are required to evaluate the feasibility of Mg ions incorporation into AFt crystals. To this end, first-principles calculations were conducted to calculate the defect formation energy (E_{def}) of Mg ion substitutions in AFt crystals:

$$E_{def}=E_1-E_0-n_1\times\mu_1+n_0\times\mu_0 \quad (2\text{-}2)$$

where, E_1 and E_0 are the total energy of the defect and perfect models, respectively. n_1 and n_0 are the number of impurity and substituent atoms. μ_1 and μ_0 stand for the chemical potentials of the impurity and substituent elements respectively. E_{def} evaluates the energetic stability of the formed defect, implying the feasibility of atomic substitution, *i.e.*, a higher E_{def} suggests a more unfavourable substitution scheme, and vice versa. Furthermore, the relationship between

E_{def} and defect concentration can be analysed to predict the uptake threshold of impurity ions in the host matrix.

In this study, we first transformed the hexagonal pristine unit cell of AFt into the orthorhombic supercell (Fig. 3) and the defect models were constructed by substituting Mg ions for Ca ions. The chemical potentials of the impurity (Mg) and substituent (Ca) ions were estimated by calculating their stable oxides. Readers are invited to refer to our previous studies for more details on the calculation of defect formation energy [35-37].

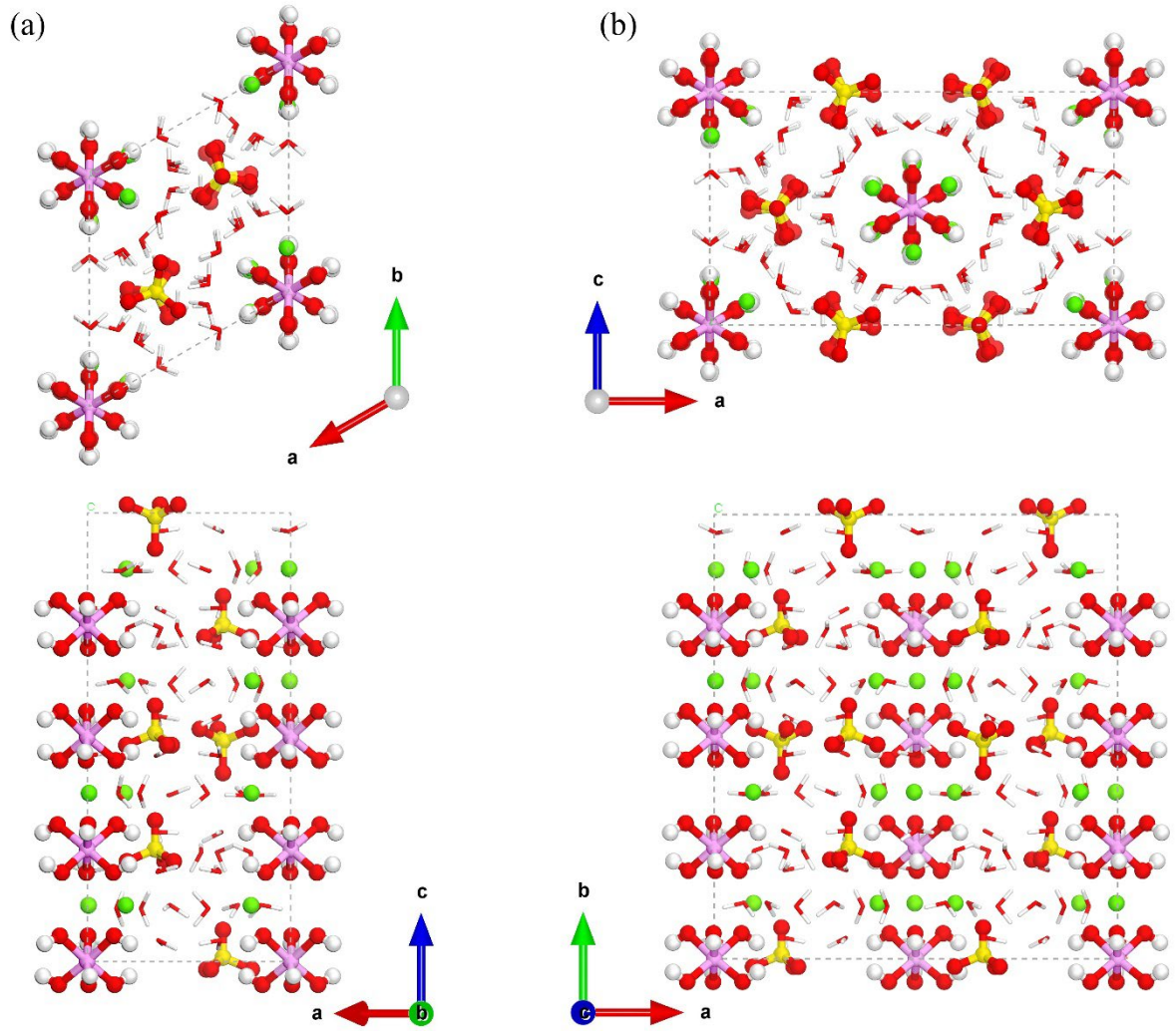

Fig. 3. Top and side views of the hexagonal unit cell (a) and orthorhombic supercell (b) of the AFt crystal. The red, yellow, pink, and green spheres stand for oxygen, sulfur, aluminum, and

calcium atoms respectively. The thin sticks gathering around the aluminate pillars are the water molecules.

The first-principles calculations were implemented with the Vienna Ab initio Simulation Package (VASP) [38, 39]. All the structural models were fully relaxed with the energy minimization method of the conjugate gradient to meet the convergence criteria of 10^{-5} eV/atom and 0.01 eV/Å for the energy and force differences respectively. The Perdew-Burke-Ernzerhof (PBE) [40] pseudopotentials with the projector augmented plane wave (PAW) [41] method were adopted to deal with the exchange-correlation interactions with a kinetic energy cut-off of 600 eV. The k-point mesh was set to 2 × 4 × 2 to evenly space the direction vectors in the reciprocal space for the orthorhombic supercells of ~ 20 Å × 11 Å × 21 Å.

2.4.2 Elastic property calculations

Since experiments and first-principles calculations confirmed that a considerable amount of Mg ions can be incorporated into AFt by substituting Ca ions (see Section 4.2), it would be of interest to understand the effect of Mg substitution on the elastic properties of AFt crystals. Herein, we calculated the elastic moduli of AFt crystals with different Mg ion contents by molecular dynamics. The pure and doped structural models of AFt were consistent with those adopted to calculate the defect formation energies (Section 2.4.1). The bulk modulus (K) and shear modulus (G) were calculated using the Hill method according to the Voight–Reuss–Hill expressions [42] and the average Young's modulus (E) was estimated through the standard relations for isotropic media:

$$E=9G/(3+G/K) \quad (2\text{-}3)$$

All structural models were first equilibrated under an isothermal-isobaric ensemble (300 K, 1 atmosphere) for 1 ns using the Nose-Hoover thermostat and barostat with a timestep of 1 fs.

Then the fully relaxed models were used to calculate the elastic tensor. The simulations were performed via the Large-scale Atomic/Molecular Massively Parallel Simulator (LAMMPS) [43] software with the PCFF_INTERFACE [44] force field, which had been intentionally modified for the cementitious minerals, *e.g.*, aluminate, portlandite, ettringite, tobermorite, *etc*.

3. Results and discussion

In ordinary Portland cements, it is well known that the hydration rate of C_3A is usually faster than that of C_3S [45]. It was reported that the AFt formed from the C_3A and gypsum can be detected after only a few minutes of hydration, whereas portlandite can be observed after about 4 h due to the hydration of C_3S [46]. In this case, the initial AFt crystals would be formed in the absence of portlandite.

Furthermore, it is noted that a shoulder peak in the calorimetry curves of some Portland cement pastes usually occurred after the main hydration peak of C_3S, which corresponded to the second hydration of C_3A to form the secondary AFt [4, 47]. Compared to the early AFt mentioned above, the secondary AFt crystals were precipitated from the pore solution containing saturated portlandite. This relatively higher OH^- concentration in the presence of portlandite compared to that in the absence of portlandite would contribute to the formation of relatively finer AFt crystals [48, 49]. Based on the above difference in the morphology of AFt formed in the solutions with lower and higher OH^- concentrations, when exploring the effect of seawater on the morphology and properties of synthetic AFt samples, two solution environments would be considered, *i.e.*, in the absence and presence of calcium hydroxide (CH) solution.

3.1. Properties characterization in the synthetic process of AFt

3.1.1. pH value evolution in the solutions

(1) In the absence of CH

The pH value evolution in the process of synthesizing the DI-AFt, SW-AFt and SW-no Mg-AFt samples during the first 2 d is shown in Fig. 4 (a). For the DI-AFt sample, the pH value rapidly increased to about 12.2 from the initial 6.3 when C_3A-gypsum powder contacted with Milli-Q water, indicating a fast dissolution of C_3A. After 8 h, the decrease in pH illustrated the precipitation of AFt crystals. Then, the continuous dissolution and precipitation processes produced more AFt, and at 28d, the pH value decreased to about 11.7.

In comparison, when seawater was used to synthesize the AFt sample (the red line in Fig. 4 (a)), the initial dissolution of C_3A elevated the pH value to about 10 from 8.1, and then there was a rapid decrease to pH=9.3. This decrease in pH was attributed to the reaction between Mg^{2+} in seawater and OH^- dissolved from C_3A, which was also found in our previous studies [9]. Then, after about 1.7 h, the pH value began to increase to 11.1 at 5 h due to the continuous dissolution of C_3A and the depletion of Mg ions in seawater. After 5 h, a more rapid decline of pH value than that in the DI-AFt solution was observed, showing a faster precipitation of AFt crystals in seawater. Besides, at about 5.5 h, there was a small shoulder peak, which displayed that the precipitation process may be accompanied by a continuous dissolution process simultaneously. After 9.2 h, the pH value decreased to about 9.8 and then slowly dropped to 9.4 at 28 d. This showed that most of the AFt were already formed within 9.2 h in seawater. Because the dissolved OH^- from C_3A would be entirely converted into AFt according to the chemical equations ((3-1) and (3-2)), the final pH should bounce back to the initial value of the solution theoretically.

$$Ca_3Al_2O_6\ (C_3A) + 6\,H_2O \rightarrow 3\,Ca^{2+} + 2\,Al(OH)_4^- + 4\,OH^- \quad (3\text{-}1)$$

$$6Ca^{2+} + 2Al(OH)_4^- + 4OH^- + 3SO_4^{2-} + 26H_2O \rightarrow 3CaO{\cdot}Al_2O_3{\cdot}3CaSO_4{\cdot}32H_2O\ (\text{AFt}) \quad (3\text{-}2)$$

When $MgCl_2$ was excluded from the simulated seawater to synthesize the AFt again, *i.e.*, the SW-no Mg-AFt sample, the trend of the pH in solution was comparable to that in DI water

in Fig. 4 (a), but its pH value was lower than that in DI-AFt sample. It is interesting to note that, when the Mg ions were not included in seawater, although the descent rate of pH value for the SW-no Mg-AFt sample was faster than that of the DI-AFt sample, it was slower than that of the SW-AFt sample.

(2) In the presence of CH

Regarding the DI-CH-AFt, SW-CH-AFt and SW-no Mg-AFt samples, the evolution trends of pH value within the first 2 d are shown in Fig. 4 (b). As for the DI-CH-AFt and SW-CH-no Mg-AFt samples, their change of pH value with reaction time was comparable with those of DI-AFt and SW-no Mg-AFt samples without CH as previously shown in Fig. 4 (a): repeated dissolution-precipitation processes. At 28 d, the pH value of DI-CH-AFt and SW-CH-no Mg-AFt samples decreased to 12.5 and 12.4. As for the SW-CH-AFt sample in Fig. 4 (b), its pH value temporarily decreased by around 0.2 at about 1 min of initial dissolution, probably due to the consumption of OH^- by Mg^{2+} in seawater. After 2 h, there was a continuous decrease in pH, indicating a continuous precipitation of AFt crystals. At 28 d of reaction, the pH value decreased to about 12.3.

Compared Fig. 4 (b) with Fig. 4 (a), it was observed that the pH values of AFt synthesized in seawater or seawater-CH solution were relatively lower than those in the corresponding DI systems. This lower pH value was also reported in the pore solution of seawater-mixed cementitious material [50]. Besides, it was observed that the pH value of SW-CH-AFt sample was higher than that of SW-CH-no Mg-AFt sample within the first 2 d, which was contrary to the corresponding AFt sample in absence of CH, *i.e.*, the pH value of the SW-AFt sample was lower than that of the SW-no-Mg-AFt sample. This reason still needs to be further explored. Additionally, as mentioned earlier, the presence of Mg species in seawater without CH seemed to cause a rapid decline of pH value during the precipitating process of AFt crystals (Fig. 4 (a)).

But when CH was present in seawater, even though Mg species also existed in the SW-CH-AFt sample, its evolution of pH value was different from that of the SW-AFt sample but similar to that of the SW-no Mg-AFt sample. The Mg species formed in both the SW-AFt and SW-CH-AFt samples will be further clarified in Section 3.1.3.

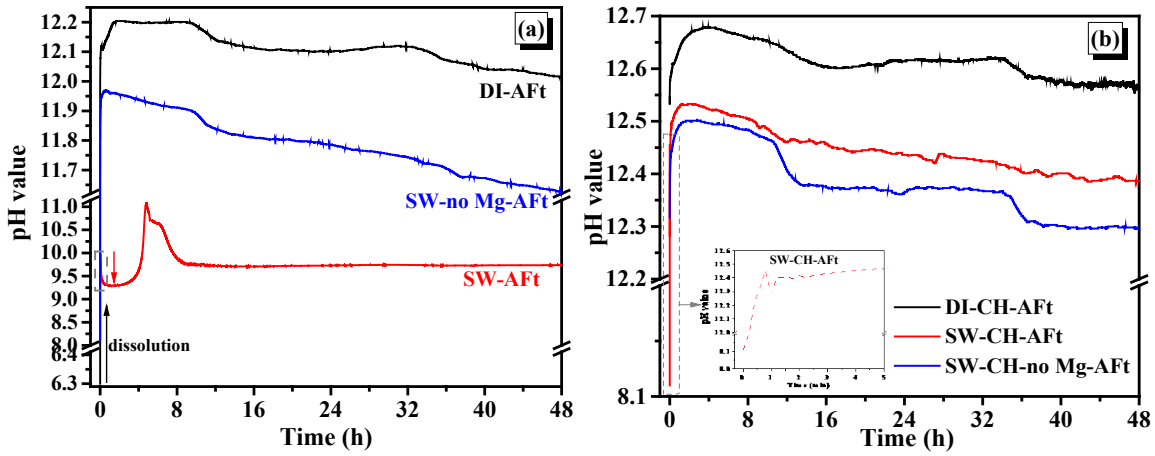

Fig. 4. Development of pH value with time for the different AFt samples. (a) is in the absence of CH, and (b) is in the presence of CH. The initial pH value of Milli-Q water and seawater solution is about 6.3 and 8.1, respectively.

3.1.2. Precipitation amount of AFt

(1) In the absence of CH

As for the DI-AFt, SW-AFt and SW-no Mg-AFt samples, the amount of AFt formed at different reaction times is displayed in Table 1. In the absence of CH, it is clear that the amount of AFt formed in the DI-AFt sample was the least from 1 d to 28 d, followed by the SW-no Mg AFt sample, and the SW-AFt sample had the highest amount of AFt. At 28 d, the AFt amount formed in the DI-AFt sample was 78 %, which was about 13 % lower than those in the SW-AFt and SW-no Mg-AFt samples. In order to maintain a comparable AFt amount, the reaction time of the DI-AFt sample was extended to 65 d.

In addition, it is noted that the AFt amount generated in the SW-AFt sample was up to 89.5 % at 1 d, which was about 2.5 to 3 times more than those AFt amounts formed in the DI-AFt and SW-no Mg-AFt samples. This rapid precipitation of AFt in the SW-AFt sample coincided with the steep decline of pH value in Fig. 4 (a).

(2) In the presence of CH

In the sat.CH environment, the amount of AFt formed in DI water and seawater at different reaction times is shown in Table 1. At 1 d, the AFt amount formed in the DI-CH-AFt sample and SW-CH-no Mg-AFt sample was similar. By contrast, there was relatively less AFt amount formed in the SW-CH-AFt sample. After 7 d, the SW-CH-no Mg-AFt sample had the highest AFt amount, followed by the SW-CH-AFt and DI-CH-AFt samples. But their difference in the formed AFt amount was not significant compared with that in the AFt samples without CH.

Table 1 AFt amount formed in the different samples at different reaction times calculated by QXRD.

		1 d	7 d	14 d	28 d	65 d
Without CH	DI-AFt	33.6	59.7	71.8	78.0	92.1
	SW-AFt	89.5	91.0	90.7	90.5	-
	SW-no Mg-AFt	36.6	70.3	83.8	91.0	-
With CH	DI-CH-AFt	21.9	52.1	73.8	80.4	-
	SW-CH-AFt	16.1	53.6	75.2	82.1	-
	SW-CH-no Mg-AFt	22.0	56.7	78.7	85.7	-

3.1.3. Analysis of reaction products through TG/DTG, DTA and FTIR

(1) In the absence of CH

Fig. 5 shows the thermogravimetric (TG/DTG) and differential thermal analysis (DTA) curves of synthetic AFt samples in the absence of CH. In Fig. 5 (a), the weight loss at ca. 100 ^{o}C and 125 ^{o}C were assigned to the water loss in AFt and gypsum, respectively. From the DTA curves highlighting the decomposition part of AFt in Fig. 5 (b), it is noted that the exothermic peak of DI-AFt crystals was at 102.0 ^{o}C. By contrast, the exothermic peaks of SW-AFt and SW-no Mg-AFt crystals were marginally shifted to relatively lower temperatures, *i.e.*, 96.4 ^{o}C and 96.9 ^{o}C, respectively.

Furthermore, compared with the DTG curves of DI-AFt and SW-no Mg-AFt samples in Fig. 5 (a), the SW-AFt sample had two peaks of weight loss probably associated with Mg-Al layered double hydroxide phase (Mg-Al LDH). The first peak at around 267 ^{o}C was ascribed to the weight loss of physical water and interlayer water, and the second peak at around 316 ^{o}C was attributed to the weight loss of main layer water and water related to the anion [51]. It was reported that the Mg-Al LDH phase was difficult to be monitored using conventional X-ray diffraction, especially at low Mg content [52], which explained why there were no corresponding peaks of the LDH phase in XRD data in Fig. S.3 (a) in the supplementary material. In addition, about 0.47 % and 0.78 % weight loss between 600 and 700 ^{o}C were related to the decomposition of carbonates in the SW-AFt and SW-no Mg-AFt samples respectively, and there was no significant weight loss in the DI-AFt sample. These carbonates generated in the SW-AFt and SW-no Mg-AFt samples were due to the introduction of HCO_3^- by seawater, *i.e.*, 0.146 g/L HCO_3^- was incorporated when preparing the simulated seawater.

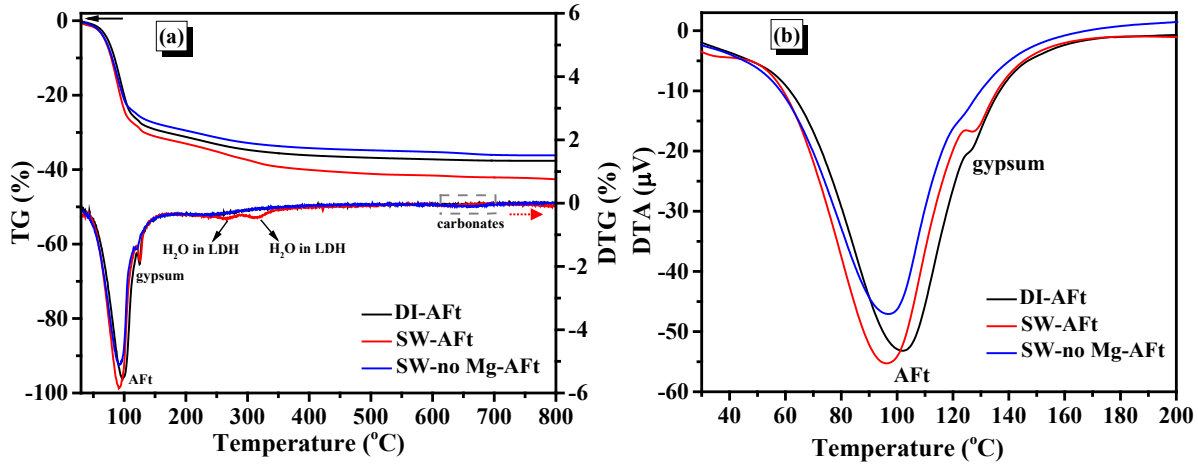

Fig. 5. (a) TG/DTG curves of the synthetic DI-AFt, SW-AFt and SW-no Mg-AFt samples at 65 d, 28 d and 28 d, respectively. (b) DTA curves of these samples highlighting the decomposition part of AFt.

(2) In the presence of CH

Figs. 6 (a)-(c) shows the TG/DTG/DTA curves of the synthetic AFt samples in different sat.CH solutions. Fig. 6 (d) presents the partial FTIR spectra of SW-CH-AFt and SW-AFt samples, and their full spectra are displayed in Fig. S.4 in the supplementary material.

In Fig. 6 (a), all the synthetic AFt samples show the water loss peaks of AFt and gypsum. From the enlarging DTA figure of AFt decomposition in Fig. 6 (b), it is found that the decomposition temperatures of AFt for the DI-CH-AFt, SW-CH-AFt, and SW-CH-no Mg-AFt samples were 102.6 ºC, 96.5 ºC, and 99.0 ºC, respectively. Compared with the AFt formed in DI-sat.CH solution, the AFt formed in the seawater environment tended to have a slightly lower decomposition temperature. This trend was consistent with those AFt formed in DI water and SW in the absence of CH (Fig. 5 (b)). In addition, the similar decomposition temperature of AFt formed in the presence and absence of CH solutions (Fig. 5 (b) vs. Fig. 6 (b)) indicated that the effect of sat.CH environment on the decomposition temperature of the formed AFt was minimal.

Except for the decomposition peaks of AFt and gypsum in Fig. 6 (a), at around 600-700 ºC, the 0.63 %, 1.44 % and 1.02 % weight loss were associated with the decomposition of carbonates in the DI-CH-AFt, SW-CH-AFt and SW-CH-no Mg-AFt samples, respectively. As mentioned above, the formation of carbonates in the AFt samples synthesized in seawater was partly due to the introduction of HCO_3^- by seawater. Besides, a small peak at around 410 ºC was assigned to the dehydroxylation of CH, and this decomposition temperature of added CH was lower than that of CH hydrated from cementitious materials, *i.e.*, at about 460 ºC [53]. Additionally, the peak at around 340 ºC in the SW-CH-AFt sample at 28 d in Fig. 6 (a) was related to the decomposition of brucite ($Mg(OH)_2$, MH). This peak was also detected in the SW-CH-AFt sample at 1 d in Fig. 6 (c), and the amount of MH was slightly decreased from 1 d to 28 d, *i.e.*, the weight loss of this dehydroxylation peak from 0.90 % to 0.72 % after recalculation based on the bound water. The FTIR spectra in Fig. 6 (d) also further verified the formation of MH in the SW-CH-AFt sample at 1 d and 28 d: anti-symmetrical O-H stretching vibration of lattice hydroxide in MH at 3700 cm^{-1} [54, 55]. Compared with the SW-CH-AFt sample at 1 d in Fig. 6 (d), the O-H bonds in MH were not observed in the spectrum of the SW-AFt sample without CH. Furthermore, a peak at around 290 ºC was also observed in the DTG curve of the SW-CH-AFt sample at 1 d in Fig. 6 (c), which was not detected in the corresponding sample at 28 d in Fig. 6 (a). This peak might be related to the dehydroxylation of $Al(OH)_3$ gel [56], which was then converted into ettringite with the reaction time [57].

Compared Fig. 5 with Fig. 6, it is noted that, in the absence of CH, the Mg ions in seawater tended to form the Mg-Al LDH phase in the SW-AFt sample, through the reaction between the Mg ions in seawater and C_3A. This phase was further verified through EDS analysis in Section 3.2.4. By contrast, when CH was present in the reaction system, brucite was precipitated in the SW-CH-AFt sample. This could be owing to the reaction between the Mg ions in seawater and

CH added, considering the relatively larger solubility product of CH compared with that of C_3A ($\log K_{sp,\,C3A}$ = -10.3 [58] vs. $\log K_{sp,\,CH}$ = -5.2 [52]).

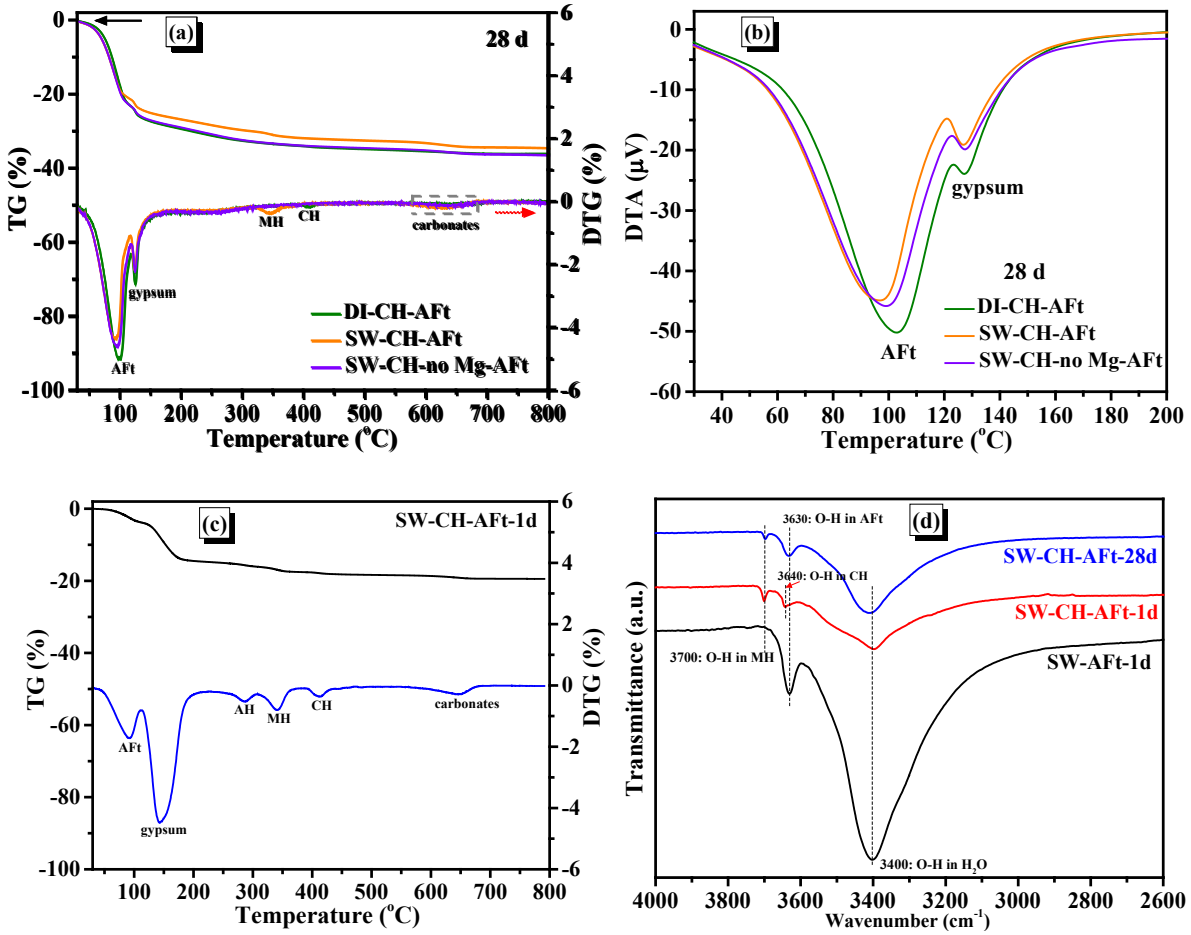

Fig. 6. (a) TG/DTG curves of the synthetic DI-CH-AFt, SW-CH-AFt and SW-CH-no Mg-AFt samples at 28 d. (b) DTA curves of these AFt samples highlighting the decomposition part of AFt. (c) TG/DTG curve of the SW-CH-AFt sample at 1 d. (d) FITR spectra of the SW-CH-AFt samples at 1 d and 28 d, and the SW-AFt sample at 1 d. MH = brucite ($Mg(OH)_2$), CH = $Ca(OH)_2$, AH=$Al(OH)_3$.

3.2. Comparison of the properties for the synthetic different AFt samples

The DI-AFt sample at 65 d and other AFt samples at 28 d were used to compare the properties of AFt samples synthesized in different DI and seawater solutions, and the

quantitative XRD analysis and qualitative XRD pattern of these samples are displayed in Table S.1 and Fig. S.3 in the supplementary material.

3.2.1. Morphology

(1) In the absence of CH

The morphologies of the synthetic DI-AFt, SW-AFt and SW-no Mg-AFt samples are presented in Figs. 7 (a)-7 (f), and the lengths of the AFt crystals are shown in Fig. 8 (a). As for the three types of AFt, a classic needle-like crystalline morphology was observed. It is noted from Figs. 7 (a)-7 (f) that the SW-AFt crystals were the longest and thickest, followed by the SW-no Mg-AFt crystals, while the DI-AFt crystals were the shortest and thinnest. From Fig. 8 (a), the median values of AFt length in the DI-AFt, SW-AFt, and SW-no Mg-AFt samples were about 1.2 μm, 11.5 μm, and 2.7 μm, respectively. Also, the length distributions of the DI-AFt and SW-no Mg-AFt were more uniform, whereas the SW-AFt crystals had a relatively wide length distribution, ranging from 2 μm to 32 μm.

The longer AFt crystals seemed to correspond to a lower pH value in Fig. 4 (a). This result agreed with those reported from Mehta [59, 60] that the larger AFt crystals with a length of 10-100 μm and several micrometres thick were normally formed in the solution with a low OH^- concentration, and the smaller AFt crystals with a length of 1-2 μm and 0.1-0.2 μm thick were formed under the condition of a higher OH^- concentration. Additionally, the relatively wider range of pH reduction in the precipitation process of AFt in the SW-AFt sample as shown in Fig. 4 (a), *i.e.*, from 11.1 to 9.4, could be responsible for its relatively wider size distribution of AFt. The reason why the OH^- concentration affected the size of the formed AFt still needs to be further explored.

(2) In the presence of CH

Figs. 7 (g) - 7 (l) and 8 (b) show the morphologies and length distribution of the synthetic AFt crystals in different sat.CH solutions. From Figs. 7 (g) - 7 (l), it is found that, in the sat.CH environment, except for the needle-like AFt, some AFt was formed in the form of granular aggregates. Besides, Fig. 8 (b) shows the median length values of AFt in the DI-CH-AFt, SW-CH-AFt, and SW-CH-no Mg-AFt samples were 0.47 μm, 0.48 μm and 0.58 μm respectively, indicating a slight difference in the length of AFt formed in DI and SW in presence of CH. As discussed above, this comparable length of AFt in these three samples could be dependent on their similar OH^- concentration in both the DI-sat.CH and SW-sat.CH solutions (Fig. 4 (b)).

When compared with the AFt grown in DI and SW without CH in Figs. 7 (a) - 7 (f) and 8 (a), it is notably found that the AFt formed in the sat.CH solution environment was relatively smaller and thinner. This was consistent with what had been reported in Ref. [60, 61].

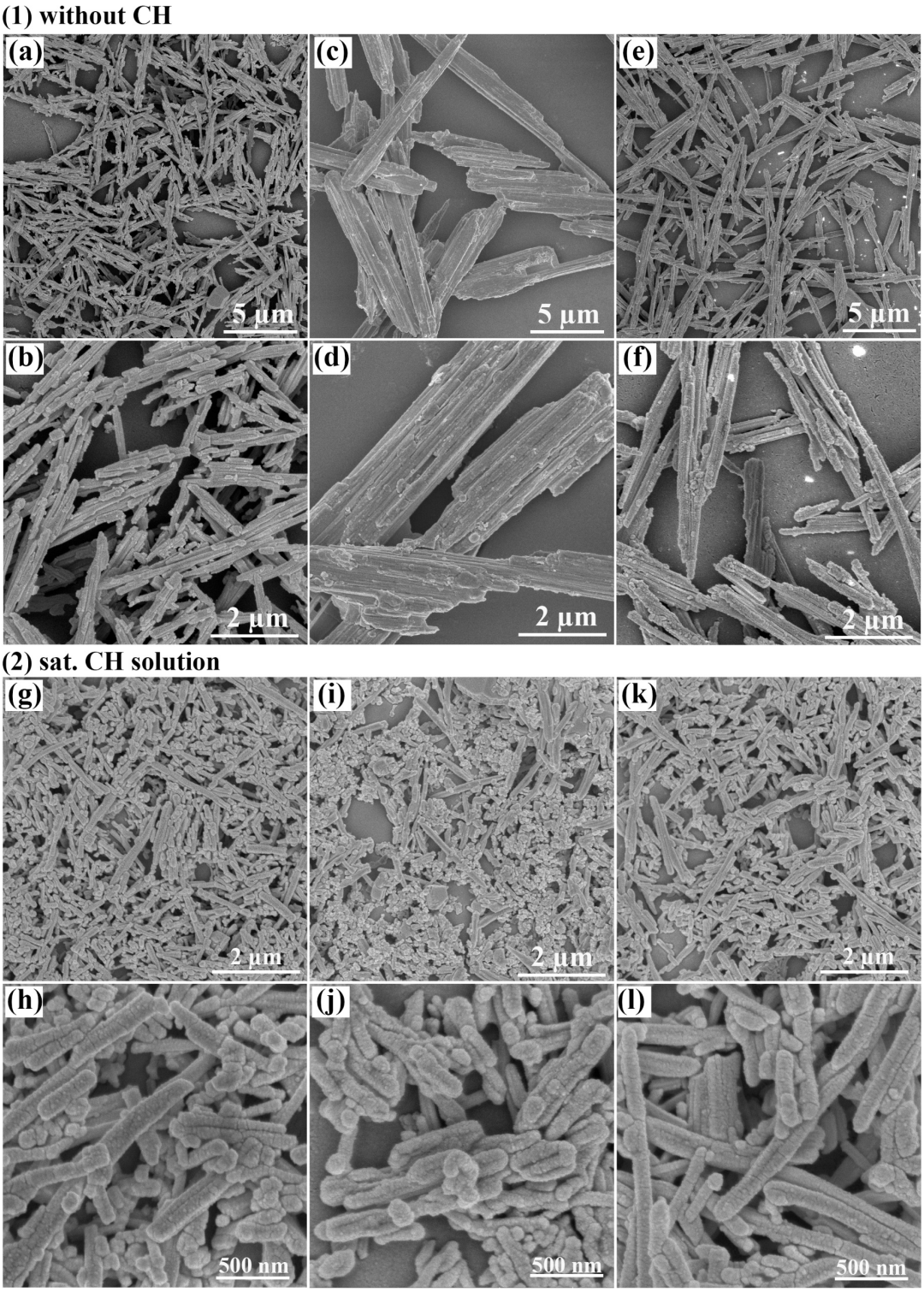

Fig. 7. Morphologies of the synthetic AFt samples. (a)-(b): DI-AFt, (c)-(d): SW-AFt, (e)-(f): SW-no Mg-AFt, (g)-(h): DI-CH-AFt, (i)-(j): SW-CH-AFt, (k)-(l): SW-CH-no Mg-AFt.

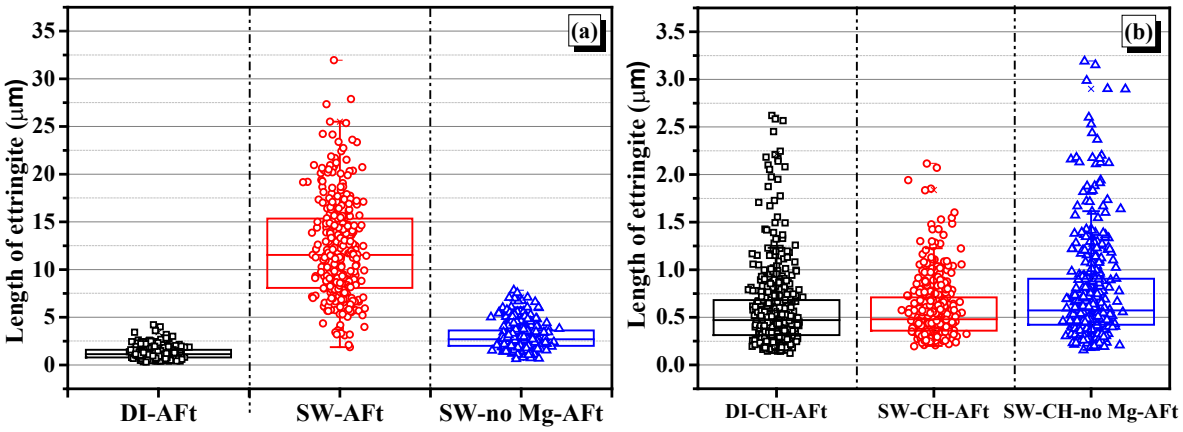

Fig. 8. Comparison of the lengths of the synthetic AFt samples. (a): the DI-AFt, SW-AFt, and SW-no Mg-AFt samples, (b) the DI-CH-AFt, SW-CH-AFt and SW-CH-no Mg-AFt samples.

3.2.2. Pore structure

(1) In the absence of CH

The pore size distributions of the synthetic DI-AFt, SW-AFt, and SW-no Mg-AFt samples are presented in Figs. 9 (a) and 9 (b). It is observed from Fig. 9 (a) that the SW-AFt sample had a relatively larger pore volume in the size range of 100 nm to 10 nm, compared with the DI-AFt and SW-no Mg-AFt samples. However, for the pores smaller than 10 nm, the increment of the pore volume in the SW-AFt sample was less than that in the DI-AFt sample. By contrast, the SW-no Mg-AFt sample displayed relatively fewer pores in both 10-100 nm and < 10 nm sizes.

From Fig. 9 (b), a much larger cumulative pore volume was noted in the SW-AFt sample, followed by the DI-AFt and SW-no Mg-AFt samples. The relatively larger cumulative pore volume in the SW-AFt sample could be attributed to its significantly more pores of size 10-100 nm in Fig. 9 (a).

(2) In the presence of CH

Figs. 9 (c) and 9 (d) shows the pore size distribution of synthetic AFt samples in different sat.CH solutions. Compared to the DI-CH-AFt sample, the SW-CH-AFt sample had relatively more pores of 10-100 nm and fewer pores of 1-10 nm in Fig. 9 (c), leading to a relatively higher cumulative pore volume in Fig. 9 (d). This feature was comparable with the SW-AFt sample in the absence of CH in Figs. 9 (a) and 9 (b). By contrast, when the Mg ions was excluded from SW-sat.CH solution, the AFt sample formed in this solution had relatively few pores of 1-100 nm and the least cumulative pore volume.

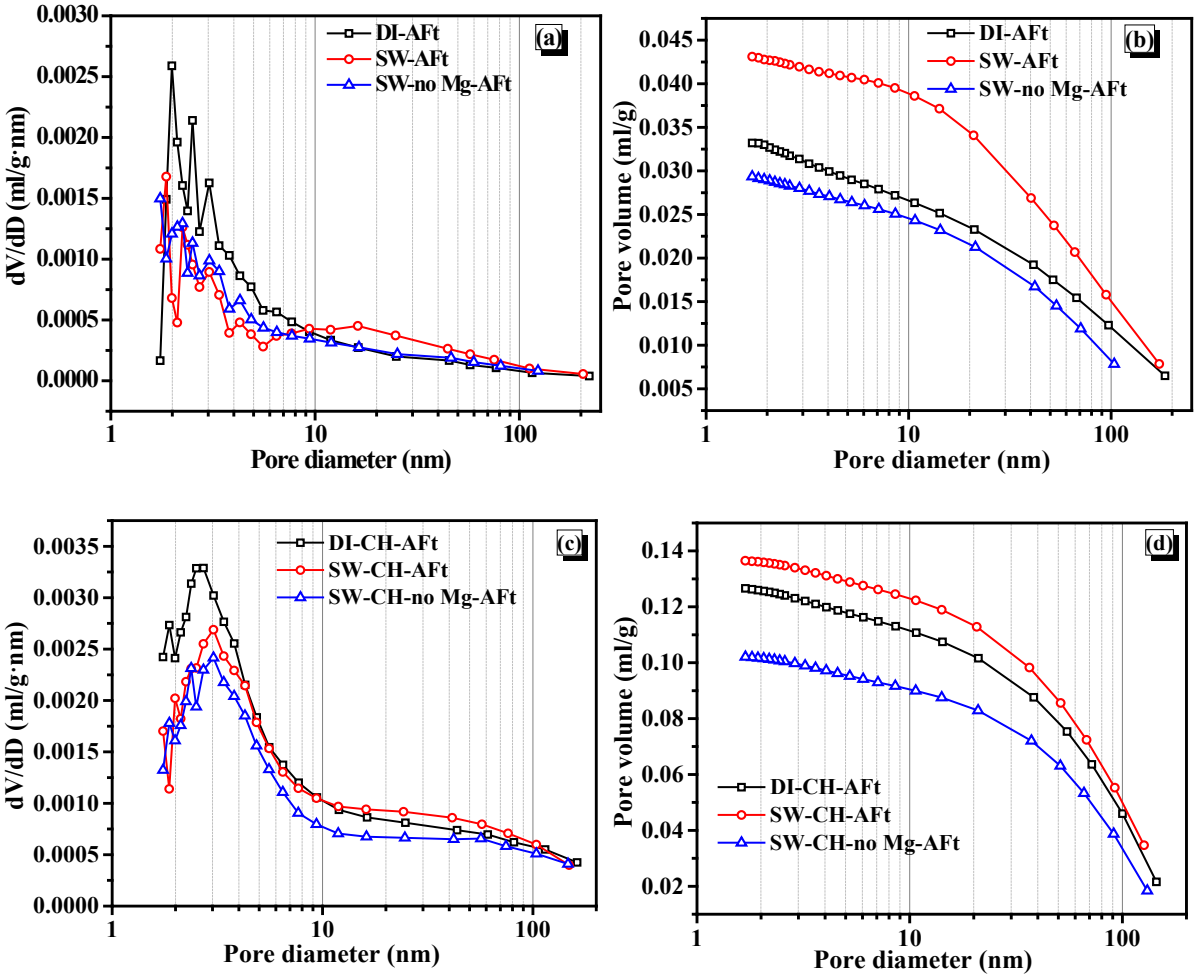

Fig. 9. Pore size distributions of the synthetic AFt samples derived from BJH analysis on nitrogen adsorption data. (a) and (b): the DI-AFt, SW-AFt, and SW-no Mg-AFt samples, (c) and (d): the DI-CH-AFt, SW-CH-AFt, and SW-CH-no Mg-AFt samples.

3.2.3. Micromechanical properties

(1) In the absence of CH

After the statistical analysis of nano-indentation data, the frequency curves of elastic modulus and hardness of the DI-AFt, SW-AFt, and SW-no Mg-AFt samples are presented in Figs. 10 (a) and 10 (b). The elastic modulus of the DI-AFt sample in Fig. 10 (a) was around 15-25 GPa. However, this modulus value for the SW-AFt sample decreased to approximately 13-22 GPa. When the $MgCl_2$ was not included in seawater, the modulus value increased to about 16-26 GPa. As for the hardness value in Fig. 10 (b), a similar trend was observed. Compared with the DI-AFt sample (0.25-0.68 GPa), the hardness of the SW-AFt sample reduced to 0.22-0.62 GPa, but the value for the SW-no Mg-AFt sample increased to 0.26-0.73 GPa.

(2) In the presence of CH

Figs. 10 (c) and 10 (d) shows the elastic modulus and hardness of the synthetic AFt samples in the sat.CH solution. From Fig. 10 (c), the elastic modulus of the DI-CH-AFt samples was around 15-32 GPa. By contrast, the SW-CH-AFt sample had a relatively lower elastic modulus, *i.e.*, 12-29 GPa. when the Mg ions were absent in seawater, the modulus of the SW-CH-no Mg-AFt sample was shifted to a relatively larger value (19-34 GPa). The same trend was also seen in the hardness value in Fig. 10 (c). The SW-CH-no Mg-AFt sample had the highest hardness value (0.47-0.93 GPa), followed by the DI-CH-AFt sample (0.19-0.94 GPa) and SW-CH-AFt sample (0.14-0.82 GPa).

By comparing Figs. 10 (a) - 10 (b) with Figs. 10 (c) - 10 (d), when CH was present, the elastic modulus and hardness of AFt were increased. This indicated that the AFt formed in the solutions with a relatively higher concentration of OH^- would have a relatively higher modulus and hardness. However, the influence of seawater on the modulus and hardness of AFt in the

sat.CH environment was similar compared to that in the absence of CH: the presence of Mg ions in seawater could lead to relatively lower elastic modulus and hardness values of the synthetic AFt samples, whereas other ions in seawater seemed to induce relatively larger elastic modulus and hardness values of AFt.

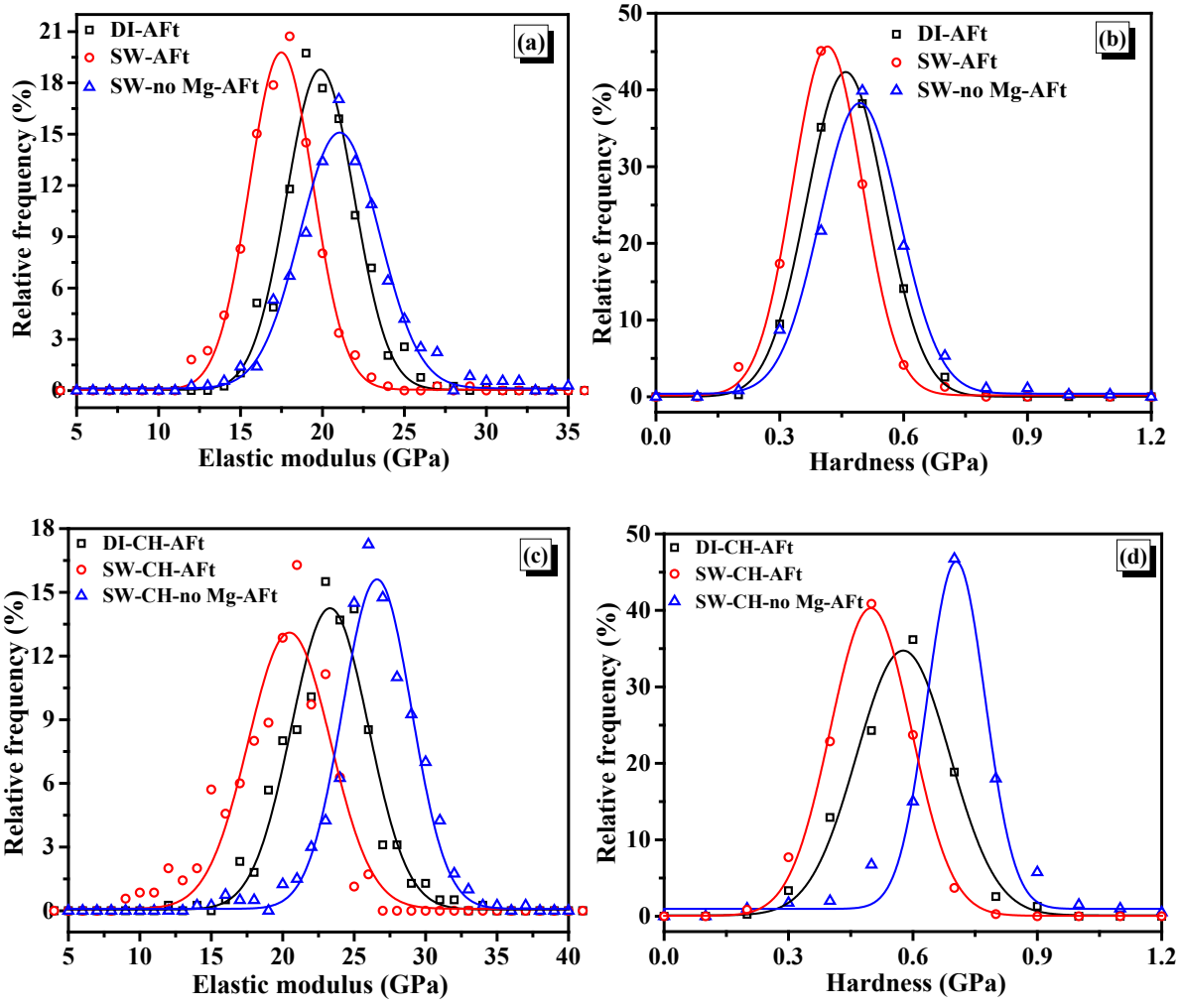

Fig. 10. Frequency plots of elastic modulus and hardness of the synthetic AFt samples. (a) and (b): the DI-AFt, SW-AFt, and SW-no Mg-AFt samples, (c) and (d): the DI-CH-AFt, SW-CH-AFt, and SW-CH-no Mg-AFt samples.

3.2.4. Elemental composition

(1) In the absence of CH

Fig. 11 shows the elemental composition of the synthetic DI-AFt, SW-AFt and SW-no Mg-AFt samples through EDS analysis. Fig. 11 (a) presents the S/Ca ratio versus the Al/Ca ratio of different synthetic AFt samples. It indicates that the DI-AFt and SW-no Mg-AFt samples had comparable S/Ca and Al/Ca ratios, which were within the range of theoretical composition of AFt crystals, *i.e.*, S/Ca~0.50 and Al/Ca~0.33. By contrast, when seawater was used to form AFt crystals, relatively higher S/Ca and Al/Ca ratios were observed (Fig. 11 (a)). It can be inferred that the Mg ions in seawater might form phases with a lower Ca content in the SW-AFt sample, but other ions in the seawater could only have a slight effect on the composition of AFt formed due to the comparable S/Ca and Al/Ca ratios in the DI-AFt and SW-no Mg-AFt samples mentioned above.

Besides, Fig. 11 (b) shows that only about 0.5 at. % (atomic percentage) of Cl was present in the SW-no Mg-AFt sample. This was consistent with the study results of Hirao et al. [62] that AFt had no binding capacity of Cl^- from external solution. By contrast, Fig. 11 (c) shows a higher atomic percentage of Cl in the SW-AFt sample, and there was an increase in the amount of Cl and a decrease in the amount of Ca, with the increase of Mg content. Considering that the Mg-Al LDH phase was monitored in the SW-AFt sample in TG data in Fig. 5 (a), it can be inferred that the new phase with a lower Ca content formed in the SW-AFt sample was Mg-Al LDH containing Cl^-.

To further verify the presence of Mg-Al LDH phase in the SW-AFt sample, the amount of Al_{res} was calculated by subtracting the theoretical value of Al_{ettr} in AFt from the total amount of Al, and then the amount of Mg versus the amount of Al_{res} is shown in Fig. 11 (d). From Fig. 11 (d), it is found that there was a linear relationship between the Mg content and Al_{res} content, and the slope and intercept were 1.97 and 0.13, respectively, *i.e.*, the average ratio of Mg/Al_{res} was approximately 2. This Mg/Al_{res} ratio was matched by that ratio reported in the Mg-Al LDH phase: the Mg-Al-LDH phase with Mg/Al ratios of 2-4 was stable [63], and a Mg-Al LDH

phase with a Mg/Al ratio of 1.4 was also synthesized in Ref. [64]. Additionally, Fig. 11 (e) displays the frequency plots of the Mg/Al_{res} ratio. It can be seen that the Mg/Al_{res} ratio between 2 or 1.5 and 4 accounted for about 50 % - 75 %. The remaining Mg ions might enter the Ca sites in the AFt structure, because the substitution behaviour also showed an inverse relationship between Mg and Ca as displayed in Fig. 11 (c). Also, this replacement was plausible due to the similar chemical characteristics of Mg and Ca [65] and a relatively smaller ionic radius of Mg [66].

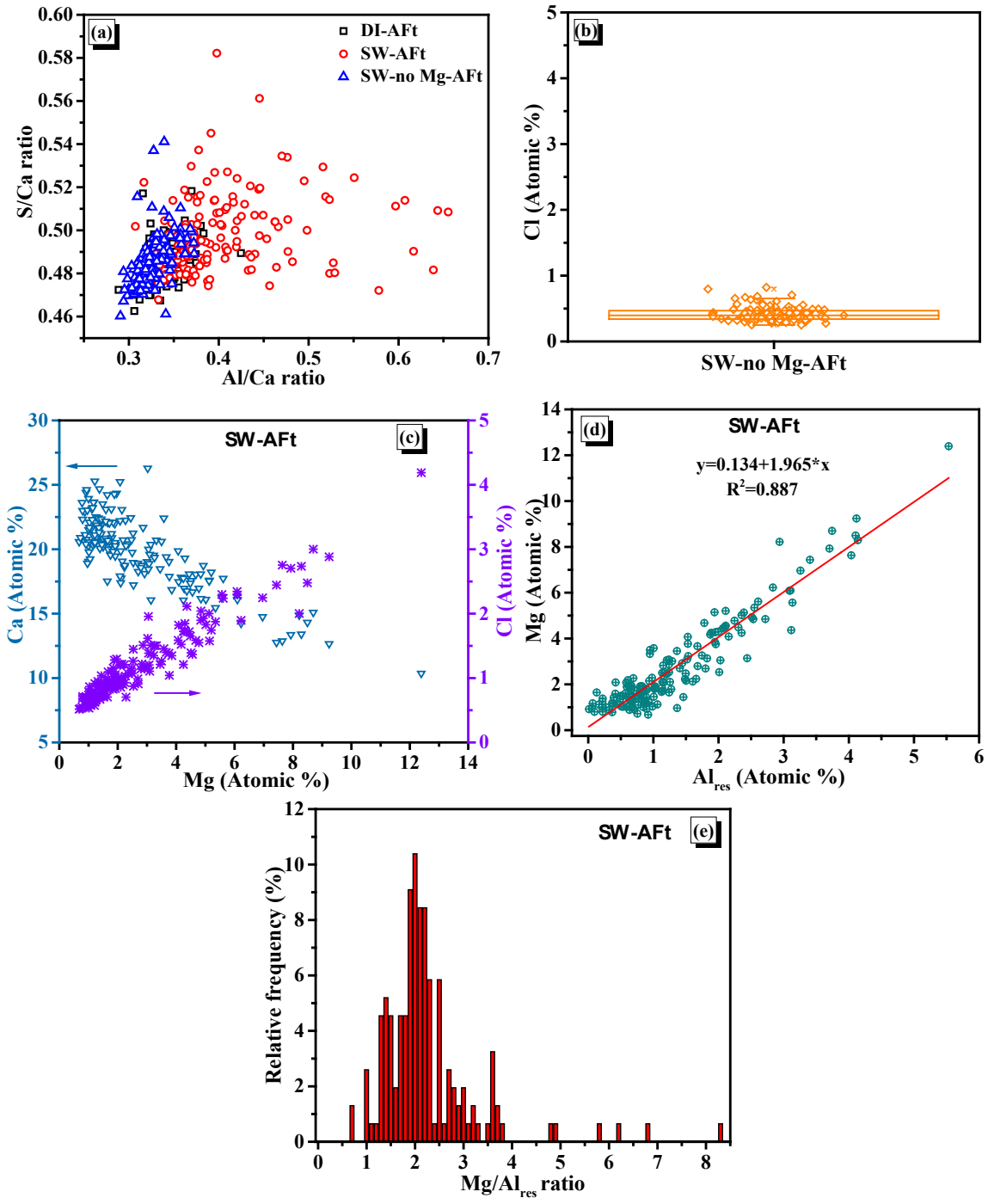

Fig. 11. SEM-EDS analytical plots of the DI-AFt, SW-AFt, and SW-no Mg-AFt samples. (a) is the S/Ca versus Al/Ca ratios of these three AFt samples. (b) is the amount of Cl in the SW-no Mg-AFt sample. (c) is the amount of Ca and Cl in the function of the amount of Mg in the SW-AFt sample. (d) is the amount of Mg versus the amount of Al_{res} that was calculated by subtracting the theoretical value of Al_{ettr} in AFt from the total amount of Al (Al_{ettr}=0.33×Ca). (e) is the frequency plots of the Mg/Al_{res} ratio.

(2) In the presence of CH

Fig. 12 (a) presents the S/Ca ratio versus the Al/Ca ratio of the synthetic AFt samples in the different sat.CH solutions. It is found that the compositions of AFt formed in the DI-CH-AFt and SW-CH-no Mg-AFt samples were comparable, which were consistent with those in the DI-AFt and SW-no Mg-AFt samples in Fig. 11 (a). By contrast, the SW-CH-AFt sample had some regions with a marginally lower S/Ca ratio and Al/Ca ratio, which was contrary to those in the SW-AFt sample without CH in Fig. 11 (a): a significant increase in both the S/Ca and Al/Ca ratios.

In addition, Fig. 12 (b) presents the atomic percentages of Ca and Cl changed with that of Mg. It is noted that the Ca amount slightly decreased with increasing Mg amount in the SW-CH-AFt sample, but the changes were significantly smaller than those in the SW-AFt sample in Fig. 11 (c). Besides, in comparison to the SW-AFt sample in Fig. 11 (c), there was no obvious increase in the Cl amount with increasing Mg content in the SW-CH-AFt sample in Fig. 12 (b). This was owing to the Mg ions in the SW-CH-AFt sample did not form the Mg-Al-Cl LDH phase, but they formed brucite. This brucite phase was detected by TG/DTG and FTIR in Figs. 6 (a), 6 (c) and 6 (d).

After calculating the Mg amount in the SW-CH-AFt sample at 1 d through TG/DTG in Fig. 6 (c), about 1.21 g Mg/100 g powder$_{(C3A+gypsum)}$ formed brucite, which was lower than the total Mg amount introduced by seawater, *i.e.*, 2.66 g Mg/100 g powder$_{(C3A+gypsum)}$. This means that, other than the formation of brucite in the SW-CH-AFt sample, about 55 % Mg ions entered the AFt structure to occupy the Ca sites. Additionally, from 1 d to 28 d, the brucite amount slightly decreased as mentioned in Section 3.1.3, *i.e.*, the amount of Mg present in the brucite decreased from 1.21 g/100 g powder$_{(C3A+gypsum)}$ to 0.97 g/100 g powder$_{(C3A+gypsum)}$. It implies that another 9 % of the total content of Mg ions were probably also incorporated into the AFt structure. This

substitution behaviour could slightly decrease the Ca content in the AFt structure (Fig. 12 (b)). But, due to a slightly excessive CH in the preparation of the SW-CH-AFt sample was introduced to increase the Ca content (Fig. S.3 (b) and Table S.1 in the supplementary material), there was no obvious increase in its S/Ca ratio and Al/Ca ratio in Fig. 12 (a).

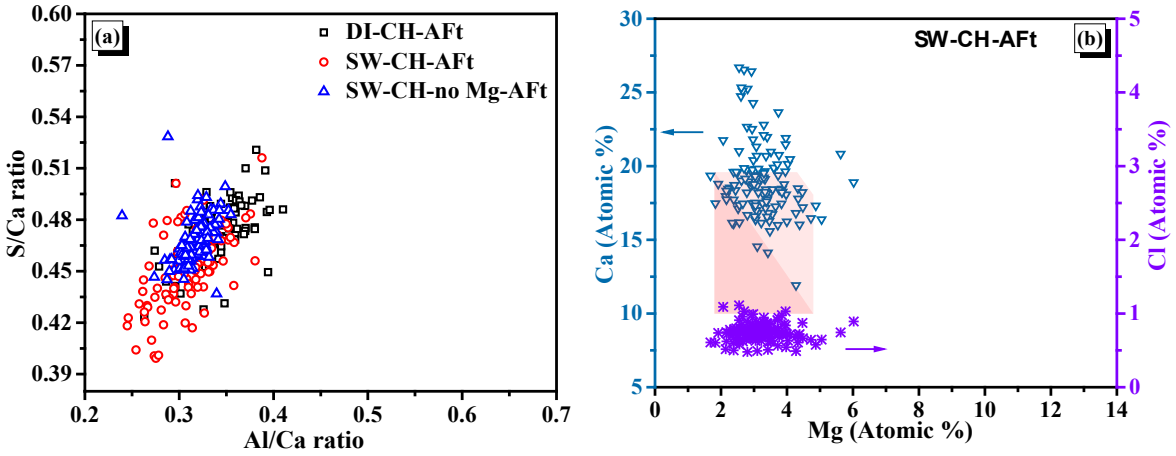

Fig. 12. EDS analytical plots of the DI-CH-AFt, SW-CH-AFt, and SW-CH-no Mg-AFt samples. (a) is the S/Ca versus Al/Ca ratios of these three AFt samples. (b) is the amount of Ca and Cl in the function of the amount of Mg in the SW-CH-AFt sample.

4. Mechanism discussion

The differences between AFt samples synthesized in the solutions with CH and without CH are compared in Table 2. The possible mechanism responsible for the different properties are further discussed in the following sections.

Table 2. Comparison of the AFt samples synthesized in different solutions.

	DI-AFt	SW-AFt	SW-no Mg-AFt	DI-CH-AFt	SW-CH-AFt	SW-CH-no Mg-AFt
Description	DI water	seawater	seawater without $MgCl_2$	DI-sat.CH solution	seawater + CH powder mixed with reactants	seawater-sat.CH solution

Important phases [a]	AFt (92 %) [b]	AFt (91 %) [b], Mg-Al-Cl LDH	AFt (91 %) [b]	AFt (80 %) [b], CH	AFt (82 %) [b], CH, $Mg(OH)_2$	AFt (86 %) [b], CH
Precipitation rate of AFt [c]	slow	very fast	fast	slow	slightly fast	fast
Elemental composition of AFt	S/Ca~0.5, Al/Ca~0.33	higher S/Ca and Al/Ca ratios	S/Ca~0.5, Al/Ca~0.33	S/Ca~0.5, Al/Ca~0.33	slightly lower S/Ca and Al/Ca ratios	S/Ca~0.5, Al/Ca~0.33
The median length of AFt (μm)	1.2	11.5	2.7	0.47	0.48	0.58
Cumulative pore volume	medium	higher, and more pores of 10-100 nm	lower	medium	higher, and more pores of 10-100 nm	lower
The decomposition temperature of AFt (°C)	102.0	96.4	96.9	102.6	96.5	99.0
Mean elastic modulus (GPa)	20 ± 2.27	17 ± 2.23	21 ± 3.31	23 ± 3.28	17 ± 2.71	27 ± 3.07
Hardness (GPa)	0.46 ± 0.09	0.42 ± 0.10	0.50 ± 0.13	0.57 ± 0.14	0.41 ± 0.11	0.69 ± 0.14

[a] Important phases analysed by QXRD and TGA were listed. Their quantitative XRD analysis is displayed in Table S.1 in the supplementary material.

[b] The numbers in the parentheses denote the amount of formed AFt at 65 d (DI-AFt sample) or 28 d (other samples) as calculated by QXRD.

[c] Precipitation rates were qualitatively compared based on the descent speed of pH values and the amount of AFt formed at different reaction times.

4.1. Effect of Mg species on the precipitation rate of AFt

According to the precipitated amount of AFt in the different solutions with and without CH in Table 1, it is evident that the precipitation rate of AFt formed in the seawater solutions was relatively faster than those in the corresponding DI water. This accelerating effect of seawater was consistent with our previous study in the C_3A-gypsum paste or C_3A-gypsum-CH paste with a water-to-solid ratio of 1: at the stage of AFt formation, the gypsum in the seawater-mixed paste was depleted at about 15 h earlier than that of the DI-mixed paste based on the

results of the calorimetric heat curves [9]. This acceleration was ascribed to the fact that, compared with DI water, the relatively higher ionic strength of seawater increased the dissolution driving force of C_3A and solubility of gypsum in seawater, especially in the absence of CH [9].

However, in this work, the Mg ions in seawater seemed to cause different precipitation rates of AFt in the presence and absence of CH. When CH was absent, the precipitation amount of AFt from seawater almost reached its maximum at 1 d (89.5 % in Table 1), which was about 2.5 times more than that from the Mg-free seawater (36.6 % in Table 1). By contrast, when CH was present, the precipitation amount of AFt from seawater and Mg-free seawater was comparable (16.1 % and 22.0 % in Table 1), and these amounts were all less than the AFt amount formed in the SW-AFt sample without CH (89.5 % in Table 1).

As mentioned in Section 3.1.3 and 3.2.4, the Mg-Al-Cl LDH phase would be formed in the SW-AFt sample, through the reaction of Mg ions in seawater and C_3A. After comparing the solubility products of the Mg-Al-Cl LDH phase and ettringite (log K $(Mg_{4.7}Al_2(OH)_{13.4}(Cl)_2 \cdot 3H_2O)$ = -56.12 and log K$(Mg_6Al_2(OH)_{16}(Cl)_2)$ = -69 [51] vs. logK (ettringite) = -44.9 [52]), the preferential precipitation of the Mg-Al-Cl LDH phase could be responsible for the subsequent rapid precipitation of AFt. Also, it has been reported that the LDH phases can shorten the setting times and increase the hydration degree of the cement paste, which was ascribed to the seeding effect of the LDH phases [67-69].

To further verify this accelerating effect of the Mg-Al LDH phase formed in the SW-AFt sample, a 5.2 g/L $MgCl_2$ solution at the same concentration as seawater was used to synthesize an AFt sample, *i.e.*, $MgCl_2$-AFt. Its pH evolution is shown in Fig. 13. It is found that the pH evolution in the $MgCl_2$-AFt sample was similar to that in the SW-AFt sample, and a slightly steeper decline of pH was observed in the $MgCl_2$-AFt sample than that in the SW-AFt sample. Besides, as for the $MgCl_2$-AFt sample, its peak II in the pH curve, *i.e.*, corresponding to the

dissolution of C_3A and the precipitation of AFt, appeared at about 1 h earlier than that in the SW-AFt sample. This indicated that the precipitation of AFt in the $MgCl_2$-AFt sample was relatively earlier and faster than that in the SW-AFt sample. After QXRD analysis, up to 87.5 % of AFt was detected in the $MgCl_2$-AFt sample at 1 d. This AFt amount was similar to that in the SW-AFt sample (89.5 %), but it was significantly higher than the AFt amount formed in $MgCl_2$-free seawater, *i.e.*, the SW-no Mg-AFt sample (36.6 %). This could be inferred that, in the absence of CH, the $MgCl_2$ in seawater played a crucial role in the accelerating precipitation of AFt, probably due to the formation of the Mg-Al LDH phase in this system.

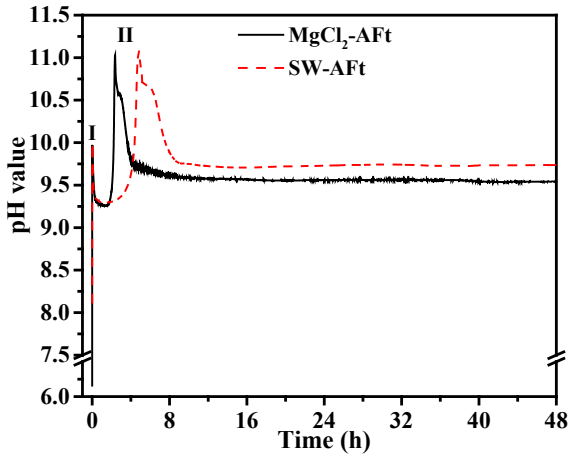

Fig. 13. pH evolution of the SW-AFt and $MgCl_2$-AFt samples. The $MgCl_2$-AFt sample denotes that the AFt sample was synthesized in a 5.2 g/L $MgCl_2$ solution. The concentration of $MgCl_2$ was the same as it was in seawater. As discussed in Section 3.1.1, peak I was related to the initial dissolution of C_3A and the precipitation of Mg species (Mg-Al LDH phase). Peak II was associated with the dissolution of C_3A and the precipitation of AFt.

4.2. The influence of Mg substitution on the stability and elastic properties of AFt crystals

The nanoindentation analyses show the Mg ions in seawater could decrease the micromechanical properties of AFt (Fig. 10), and the elemental analyses suggest that this

reduction might be ascribed to the Mg incorporation in the AFt crystals (Figs. 11 (c) and 12 (b)). Previous studies proposed the possible atomic substitution of Ca in the AFt crystal by Mg, by comparing their ionic radius [20, 34]. Indeed, the similarity of atomic radius and electronic structures always governs the atomic substitution preference [36, 37], and the substitution of Ca by Mg has been widely accepted for the clinker phases [70] and hydration products [71]. While experimental studies usually estimate the atomic substitution by spectroscopic or compositional analyses, the energetic evaluation by accurate ab initio calculations is a desirable supplementary verification [35, 72]. Here, the defect formation energy calculations were performed to provide an energetic evaluation of Mg substitution in the AFt crystals. The Mg content in the calculation is defined as the atomic percentage, *i.e.*, Mg/(Mg+Ca), to be consistent with the experimental data. Fig. 14 (a) shows an E_{def} of 0.54 eV at the Mg content of 4.2 %. This level of energy barrier supported the energetic feasibility of Mg substitution in AFt compared to the E_{def} magnitude of impurity ions in clinker crystals [35-37]. On the other hand, a positive E_{def} suggested that Mg substitution was detrimental to crystal stability, which partially explains the slight decrease in the decomposition temperature of AFt formed in seawater (Table 2). The detrimental effect on AFt crystal stability was enhanced with increasing Mg content, which in turn determined the upper limit of the Mg content in the AFt crystals. The increase rates of normalized E_{def} ($Norm\_E_{def}$, $Norm\_E_{def} = E_{def}$ / Mg content) with Mg content were calculated by finite difference as shown in Fig. 14 (b). The first local minimum was at the Mg content of 12.5 %, after which $Norm\_E_{def}$ increased rapidly with Mg content. Therefore, 12.5 % can be roughly considered as a theoretical threshold for the Mg content in AFt, within which the crystal stability would not be significantly destroyed. The second minimum at the Mg content of 25 % was of similar significance, the accumulative E_{def} at this Mg content however was more than 5 eV, which was energetically prohibitive.

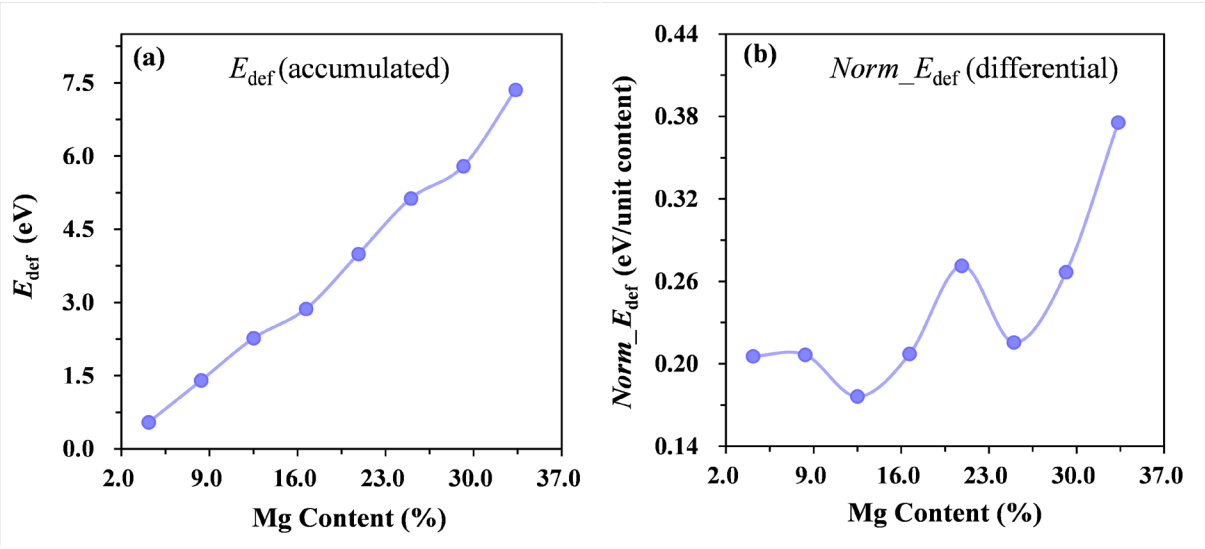

Fig. 14. Calculated defect formation energies of different Mg dosages in AFt. (a): the accumulated defect formation energy calculated directly from Equation (2-2). (b): the defect formation energy differential. The Mg content is defined as the atomic percentage, *i.e.*, Mg/(Mg+Ca).

Since it has been demonstrated that Mg could partially replace Ca in AFt crystals, a naturally raised question is how the Mg substitution would affect the mechanical properties of AFt crystals. Based on the molecular dynamic calculations, it is found that, within a certain range, the Young's modulus of the Mg-doped AFt crystal was similar to or slightly higher than that of the pure AFt crystal (Fig. 15). This was understandable as the strength of Mg-O bonds introduced by Mg-doping was higher than that of original Ca-O bonds. However, when the Mg dosage exceeded 12.5 %, the Young's modulus of the defect AFt crystal decreased dramatically, and the standard deviation increased strikingly. This indicated that the high Mg intake destroyed the stability and enhanced the anisotropy of the AFt crystal. The analysis from the defect formation energy above suggested that 12.5 % might be the threshold for the Mg substitution, and the calculation of the elastic moduli here also supported this prediction.

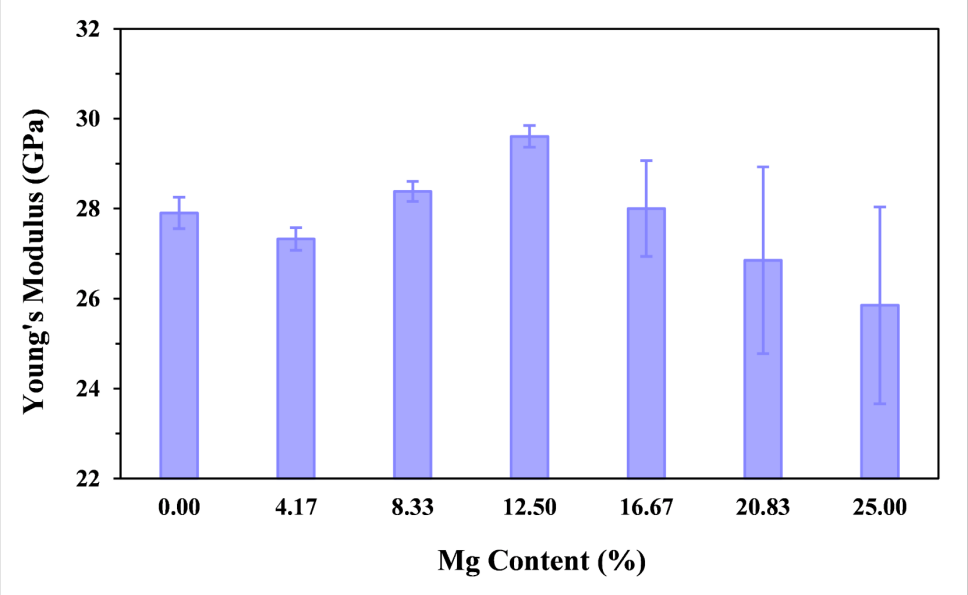

Fig. 15. Calculated Young's modulus of pure and Mg-doped AFt crystals. Each group contains 40 tests with strains from 10^{-3} to 10^{-2}. The Mg content is defined as the atomic percentage, *i.e.*, Mg/(Mg+Ca).

4.3. The effect of packing density of AFt particles on the micromechanical property

It was reported that the micromechanical behaviour was governed by the packing density ('one minus porosity') distribution of particles [29, 73]. From Figs. 16 (a) - (d), it is noted that the indentation modulus and hardness of samples would increase with the increase of packing density, revealing a positive correlation relationship between indentation modulus, hardness, and packing density. Hence, the larger modulus and hardness of the AFt synthesized in Mg-free seawater, *i.e.*, the SW-no Mg-AFt and SW-CH-no Mg-AFt samples (Fig. 10), could be attributed to their higher packing density in Figs. 16 (e) and 16 (f). The relatively smaller cumulative pore volume of the SW-no Mg-AFt and SW-CH-no Mg-AFt samples (Fig. 9) also further supported the higher packing density. This demonstrated that, besides the Mg ions, other ions in seawater could contribute to a larger packing density of AFt formed, further leading to the improvement of the micromechanical properties. But this reason still needs to be further explored.

In addition, when the AFt was formed in seawater containing Mg ions, *i.e.*, the SW-AFt and SW-CH-AFt samples, the lower modulus and hardness (Fig. 10) could be ascribed to their lower packing density (Figs. 16 (e) and 16 (f)). The relatively larger cumulative pore volume of the SW-AFt and SW-CH-AFt samples, especially more pores between 10 and 100 nm (Fig. 9), likewise threw light on their lower packing density. The possible reasons for the lower packing density of AFt samples synthesized in seawater with Mg ions were ascribed to the following two aspects.

1) Relatively larger crystal size of AFt

Table 3 illustrates that the crystal size of AFt in the SW-AFt sample was larger than the other AFt samples. These large crystals would lead to a low packing density due to the consequent larger voids between the crystals [74].

2) Unstable AFt structure due to the substitution of Ca by Mg

The intrinsic solid stiffness (m_s) of AFt can be derived from the fitted curve between the indentation modulus and packing density in Figs. 16 (a) and 16 (c). The m_s can be defined as the asymptotic contact modulus when packing density approaches 1, *i.e.*, $m_s=\lim_{\eta=1}M$. The m_s values of synthetic different AFt samples and the corresponding intrinsic elastic modulus (E_s) are listed in Table 4. It can be observed that the m_s values of the SW-AFt and SW-CH-AFt samples decreased by ~ 6 % and ~ 10 % respectively, compared with the DI-AFt and DI-CH-AFt samples. A similar reduction trend of E_s for the SW-AFt and SW-CH-AFt samples can also be seen. This decrease of elastic modulus, E_s, could be related to the Mg replacement in the AFt structure. As discussed in Section 4.2, a higher than 12.5 % of Mg content in AFt would lead to an unstable structure and then a reduction of elastic modulus (Fig. 15). Based on EDS results, the average values of Mg substitution in the SW-AFt and SW-CH-AFt samples were estimated to be roughly ~10 % and ~14.5 %, respectively (Fig. 17). But the mean value of Mg replacement in the SW-AFt sample could be underestimated due to the possible overestimation

of Mg content present in the Mg-Al-Cl LDH phase. Besides, the Mg replacement amount in the SW-CH-AFt sample could be overestimated owing to the presence of little brucite in this sample at 28 d (Fig. 6 (a)). Much more relevant experiments are still needed to provide more evidence for this substitution behaviour.

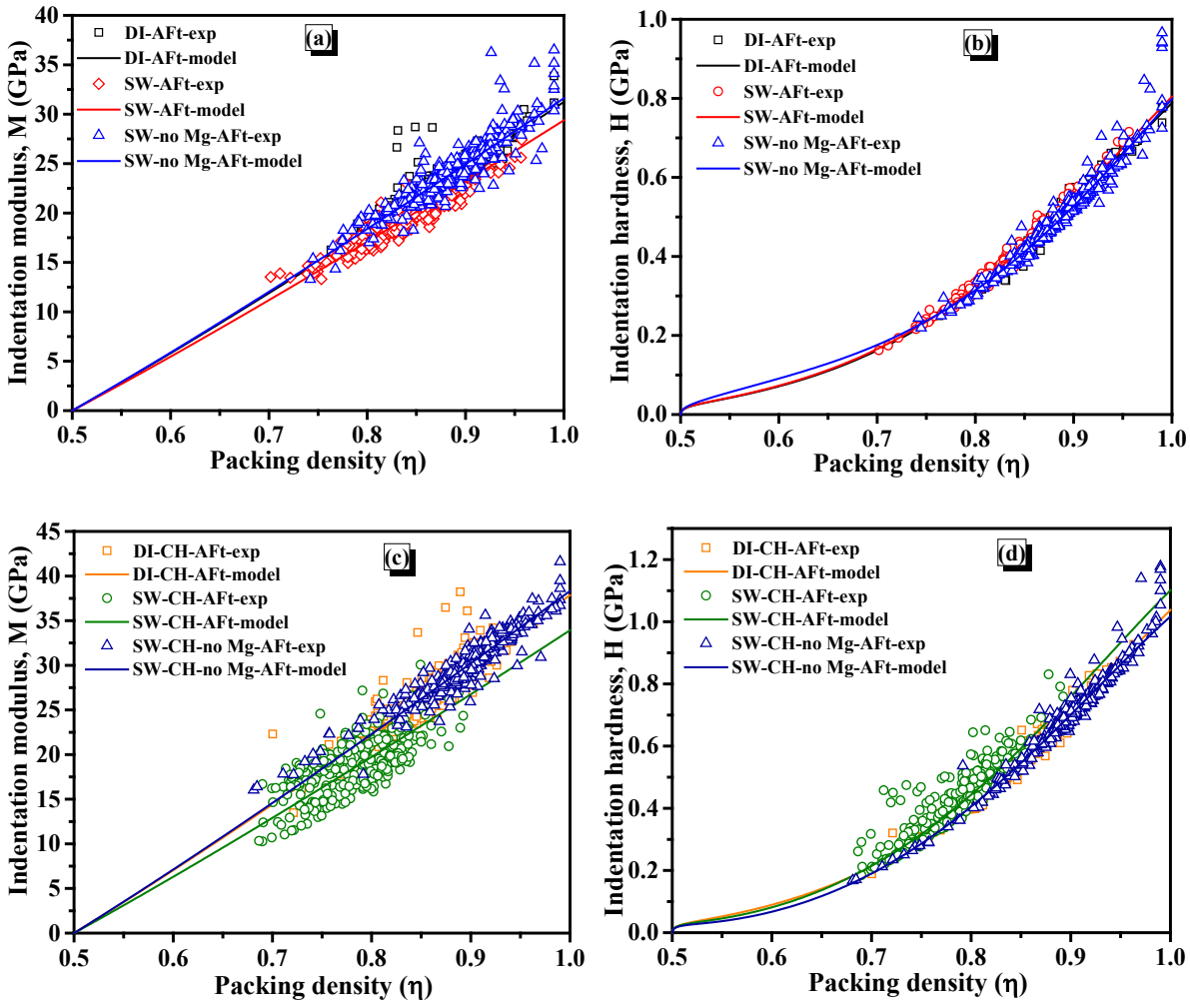

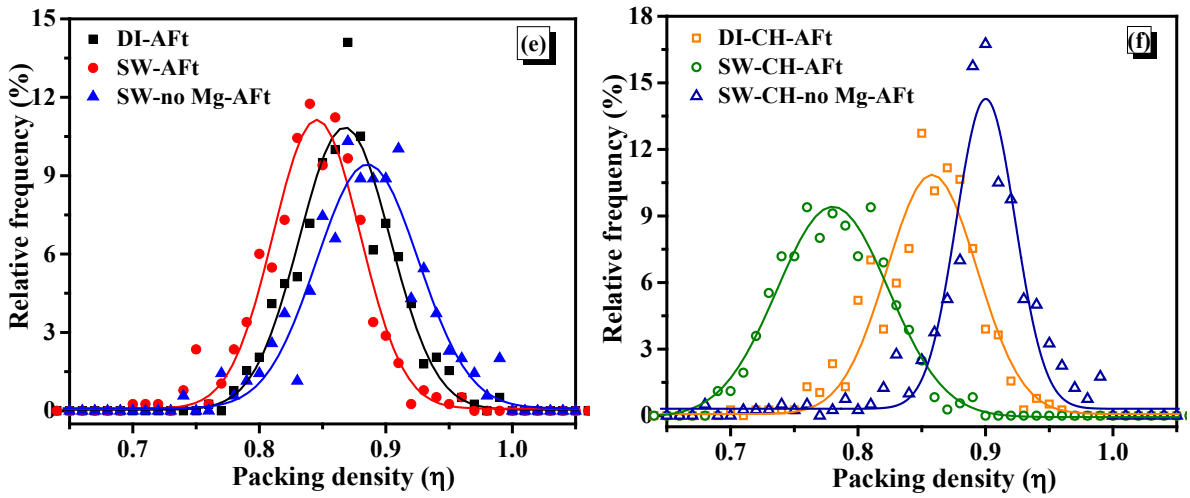

Fig. 16. Packing density scaling relations of indentation modulus ((a) and (c)) and hardness ((b) and (d)), which are obtained from nanoindentation tests. (e) and (f) are the frequency plots of the packing density of the synthetic AFt samples. (a), (b), and (e) were the synthetic AFt samples in the absence of CH, and (c), (d), and (f) are the synthetic AFt samples in the presence of CH.

Table 3. Crystal size of the synthetic AFt crystals.

Sample name	Crystal size (Å)
DI-AFt	300 ± 11.5
SW-AFt	360 ± 10.0
SW-no Mg-AFt	301 ± 15.8
DI-CH-AFt	289 ± 19.1
SW-CH-AFt	291 ± 23.1
SW-CH-no Mg-AFt	289 ± 20.8

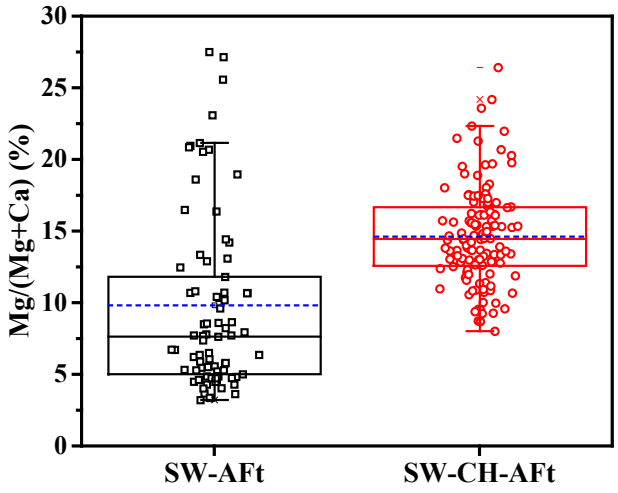

Fig. 17. Substitution amount of Ca by Mg in the SW-AFt and SW-CH-AFt samples. The blue dashed lines represent the mean values. Due to the presence of Mg-Al-Cl-LDH in the SW-AFt sample, it was difficult to identify exactly which Mg entered the AFt structure. According to Fig. 11 (e), the EDS data points for which the Mg/Al_{res} ratios did not fall between 2-4 were selected.

Table 4. Intrinsic stiffness (m_s) and elastic modulus (E_s) of the synthetic AFt samples.

Sample name	intrinsic stiffness (m_s)	intrinsic elastic modulus (E_s)
DI-AFt	31.3	28.4
SW-AFt	29.4	26.7
SW-no Mg-AFt	31.6	28.8
DI-CH-AFt	37.9	34.6
SW-CH-AFt	33.9	30.9
SW-CH-no Mg-AFt	38.3	35.1

Note: the elastic modulus (E_s) can be calculated using the equation, *i.e.*, $E_s = m_s \times (1-v_s)$. where v_s denotes the Poisson' ratio of AFt, and a 0.34 of v_s was used as described in Section 2.3.3.

5. Conclusions and outlook

This work investigated the effect of seawater on the growth rate, morphology, pore structure, and micromechanical property of the synthetic AFt by using different experimental characterization methods, *i.e.*, XRD, SEM, nano-indentation, BET, pH meter, TG/DTA and FTIR. Furthermore, atomistic simulations were employed to evaluate the feasibility of Mg ions incorporation into the AFt structure and the influence of Mg substitution on the elastic properties of AFt crystals. The main findings from the present work are summarized as follows:

- In the absence of CH, the partial Mg ions in seawater would preferentially form the Mg-Al-Cl LDH phase, which would accelerate the subsequent precipitation of AFt crystals in the SW-AFt sample compared with that in the SW-no Mg-AFt sample. By contrast, in the presence of CH, the partial Mg ions in seawater would form brucite rather than the Mg-Al-Cl LDH phase. Probably, for this reason, the precipitation rates of AFt in the SW-CH-AFt and SW-CH-no Mg-AFt samples were comparable.
- The AFt grown in seawater had a relatively larger cumulative pore volume and lower packing density compared with the corresponding AFt formed in DI water, leading to a relatively lower elastic modulus and hardness. This could be mainly ascribed to some Mg ions in seawater entered the sites of Ca ions in AFt, leading to a relatively unstable structure.
- When Mg ions were excluded from seawater, it was found that other ions in seawater did not change the chemical composition of AFt, and the AFt formed in this Mg-free seawater had a smaller cumulative pore volume and higher packing density, compared with the corresponding AFt grown in DI water. This would result in a higher elastic modulus and hardness.

The current study results have suggested that the AFt grown in seawater-mixing cement and concrete could have poorer micromechanical properties. This finding may also give us more information on the degradation of cement and concrete exposed to the seawater environment from the perspective of aluminate phases in cement.

Regarding the seawater erosion on cement and concrete, the deterioration of mechanical properties was mainly attributed to the calcium leaching, degradation of C-S-H gel and the expansion cracks due to the formation of AFt and gypsum [75, 76]. However, this finding in this work, *i.e.*, the decrease in elastic modulus and hardness of AFt caused by the incorporation of Mg ions in AFt, might also be one of the reasons for the disintegration of cement and concrete subjected to seawater erosion. Additionally, more investigations are needed to gain an understanding of the expansive property of Mg-doped AFt, which is also a vital concern for the durability of cement and concrete.

Acknowledgments

The authors would like to acknowledge the financial support by the Research Grants Council of the Hong Kong SAR Government (Project No. T22-502/18-R), the Research Centre for Resources Engineering towards Carbon Neutrality (RCRE) and The Hong Kong Polytechnic University. The first author is also grateful to Dr. Yongqiang Li and Dr. Xiaohong Zhu for their help with the calculation of crystal size and TG test.

Reference

[1] Y.L. Li, X.L. Zhao, R.S. Raman, Durability of seawater and sea sand concrete and seawater and sea sand concrete–filled fibre-reinforced polymer/stainless steel tubular stub columns, Adv. Struct. Eng. 24 (2021) 1074-1089.

[2] W. Xin, S. Jianzhe, D. Lining, J. Yundong, W. Zhishen, Durability of coral-reef-sand concrete beams reinforced with basalt fibre-reinforced polymer bars in seawater, Adv. Struct. Eng. 24 (2021) 1235-1247.

[3] A. Ahmed, S. Guo, Z. Zhang, C. Shi, D. Zhu, A review on durability of fiber reinforced polymer (FRP) bars reinforced seawater sea sand concrete, Constr. Build. Mater. 256 (2020) 119484.

[4] P. Li, W. Li, T. Yu, F. Qu, V.W.Y. Tam, Investigation on early-age hydration, mechanical properties and microstructure of seawater sea sand cement mortar, Constr. Build. Mater. 249 (2020) 118776.

[5] L. Montanari, P. Suraneni, M. Tsui-Chang, M. Khatibmasjedi, U. Ebead, J. Weiss, A. Nanni, Hydration, Pore Solution, and Porosity of Cementitious Pastes Made with Seawater, J. Mater. Civ. Eng. 31 (2019) 04019154.
[6] J. Wang, E. Liu, L. Li, Multiscale investigations on hydration mechanisms in seawater OPC paste, Constr. Build. Mater. 191 (2018) 891-903.
[7] W.L. Lam, P. Shen, Y. Cai, Y. Sun, Y. Zhang, C.S. Poon, Effects of seawater on UHPC: Macro and microstructure properties, Constr. Build. Mater. 340 (2022) 127767.
[8] Y. Sun, Y. Zhang, Y. Cai, W.L. Lam, J.X. Lu, P. Shen, C.S. Poon, Mechanisms on accelerating hydration of alite mixed with inorganic salts in seawater and characteristics of hydration products, ACS Sustain. Chem. Eng. 9 (2021) 10479-10490.
[9] Y. Cai, D. Xuan, C.S. Poon, Influence of availability of calcium on the hydration of tricalcium aluminate (C_3A) in seawater mixed C_3A-gypsum system, J. Am. Ceram. Soc. 105 (2022) 5895-5910.
[10] Y. Sun, J.-X. Lu, P. Shen, C.S. Poon, Hydration kinetics and microstructure evolution of NaCl-mixed tricalcium silicate pastes, Cem. Concr. Res. 161 (2022) 106934.
[11] C.W. Hargis, A.P. Kirchheim, P.J. Monteiro, E.M. Gartner, Early age hydration of calcium sulfoaluminate (synthetic ye'elimite, C_4A_3S) in the presence of gypsum and varying amounts of calcium hydroxide, Cem. Concr. Res. 48 (2013) 105-115.
[12] P. Mehta, Scanning electron micrographic studies of ettringite formation, Cem. Concr. Res. 6 (1976) 169-182.
[13] F. Winnefeld, B. Lothenbach, Hydration of calcium sulfoaluminate cements—Experimental findings and thermodynamic modelling, Cem. Concr. Res. 40 (2010) 1239-1247.
[14] M. García-Maté, A. De la Torre, L. León-Reina, M. Aranda, I. Santacruz, Hydration studies of calcium sulfoaluminate cements blended with fly ash, Cem. Concr. Res. 54 (2013) 12-20.
[15] J. Yu, J. Qian, J. Tang, Z. Ji, Y. Fan, Effect of ettringite seed crystals on the properties of calcium sulphoaluminate cement, Constr. Build. Mater. 207 (2019) 249-257.
[16] L. Fernández-Carrasco, E. Vázquez, Reactions of fly ash with calcium aluminate cement and calcium sulphate, Fuel, 88 (2009) 1533-1538.
[17] M. Santhanam, M.D. Cohen, J.J.C. Olek, Sulfate attack research—whither now?, Cem. Concr. Res. 31 (2001) 845-851.
[18] R. Ragoug, O.O. Metalssi, F. Barberon, J.-M. Torrenti, N. Roussel, L. Divet, J.-B.d.E. de Lacaillerie, Durability of cement pastes exposed to external sulfate attack and leaching: Physical and chemical aspects, Cem. Concr. Res. 116 (2019) 134-145.
[19] H. Taylor, C. Famy, K. Scrivener, Delayed ettringite formation, Cem. Concr. Res. 31 (2001) 683-693.
[20] A. Cody, H. Lee, R. Cody, P. Spry, The effects of chemical environment on the nucleation, growth, and stability of ettringite $[Ca_3Al(OH)_6]_2(SO_4)_3 \cdot 26H_2O$, Cem. Concr. Res. 34 (2004) 869-881.

[21] Y. Cai, D. Xuan, P. Hou, J. Shi, C.S. Poon, Effect of seawater as mixing water on the hydration behaviour of tricalcium aluminate, Cem. Concr. Res. 149 (2021) 106565.
[22] A. Standard, D1141-98: Standard Practice for the Preparation of Substitute Ocean Water, ASTM International, West Conshohocken, 2013.
[23] M. Miller, C. Bobko, M. Vandamme, F.-J. Ulm, Surface roughness criteria for cement paste nanoindentation, Cem. Concr. Res. 38 (2008) 467-476.
[24] Y. Sun, J.X. Lu, C.S. Poon, Strength degradation of seawater-mixed alite pastes: an explanation from statistical nanoindentation perspective, Cem. Concr. Res. 152 (2022) 106669.
[25] Bruker TI Premier user manual, (2018) 173-175.
[26] L. Liu, A. Jaramillo-Botero, W.A. Goddard III, H. Sun, Development of a ReaxFF reactive force field for ettringite and study of its mechanical failure modes from reactive dynamics simulations, J. Phys. Chem. A, 116 (2012) 3918-3925.
[27] S. Speziale, F. Jiang, Z. Mao, P.J. Monteiro, H.-R. Wenk, T.S. Duffy, F.R. Schilling, Single-crystal elastic constants of natural ettringite, Cem. Concr. Res. 38 (2008) 885-889.
[28] T. Honorio, P. Guerra, A. Bourdot, Molecular simulation of the structure and elastic properties of ettringite and monosulfoaluminate, Cem. Concr. Res. 135 (2020) 106126.
[29] F.J. Ulm, M. Vandamme, C. Bobko, J. Alberto Ortega, K. Tai, C. Ortiz, Statistical indentation techniques for hydrated nanocomposites: concrete, bone, and shale, J. Am. Ceram. Soc. 90 (2007) 2677-2692.
[30] E.P. Barrett, L. Joyner, P. Halenda, Granular Adsorbents for Sugar Refining. Some Factors Affecting Porosity and Activity in Service, Ind. Eng. Chem. 44 (1952) 1827-1833.
[31] K.S. Sing, Physisorption of nitrogen by porous materials, J. Porous Mater. 2 (1995) 5-8.
[32] J. Olek, T. Kim, Effects of Sample Preparation and Interpretation of Thermogravimetric Curves on Calcium Hydroxide in Hydrated Pastes and Mortars, Transport. Res. Rec.: J. Transport. Res. Board, 2290 (2012) 10-18.
[33] K. Scrivener, R. Snellings, B. Lothenbach, A practical guide to microstructural analysis of cementitious materials, Crc Press, (2018) 196-200.
[34] V. Albino, R. Cioffi, M. Marroccoli, L. Santoro, Potential application of ettringite generating systems for hazardous waste stabilization, J. Hazard. Mater. 51 (1996) 241-252.
[35] Y. Tao, N. Li, W. Zhang, F. Wang, S. Hu, Understanding the zinc incorporation into silicate clinker during waste co-disposal of cement kiln: A density functional theory study, J. Clean. Prod. 232 (2019) 329-336.
[36] Y. Tao, W. Zhang, D. Shang, Z. Xia, N. Li, W.-Y. Ching, F. Wang, S. Hu, Comprehending the occupying preference of manganese substitution in crystalline cement clinker phases: A theoretical study, Cem. Concr. Res. 109 (2018) 19-29.
[37] Y. Tao, W. Zhang, N. Li, D. Shang, Z. Xia, F. Wang, Fundamental principles that govern the copper doping behavior in complex clinker system, J. Am. Ceram. Soc. 101 (2018) 2527-2536.

[38] G. Kresse, J. Furthmüller, Efficiency of ab-initio total energy calculations for metals and semiconductors using a plane-wave basis set, Comp. Mater. Sci. 6 (1996) 15-50.
[39] G. Kresse, J. Hafner, Ab initio molecular dynamics for liquid metals, Phys. Rev. B 47 (1993) 558.
[40] J.P. Perdew, K. Burke, M. Ernzerhof, Generalized gradient approximation made simple, Phys. Rev. Lett. 77 (1996) 3865.
[41] P.E. Blöchl, Projector augmented-wave method, Phys. Rev. B 50 (1994) 17953.
[42] R. Hill, The elastic behaviour of a crystalline aggregate, Proc. Phys. Soc. A 65 (1952) 349.
[43] S. Plimpton, Fast parallel algorithms for short-range molecular dynamics, J. Comput. Phys. 117 (1995) 1-19.
[44] H. Heinz, T.-J. Lin, R. Kishore Mishra, F.S. Emami, Thermodynamically consistent force fields for the assembly of inorganic, organic, and biological nanostructures: the INTERFACE force field, Langmuir, 29 (2013) 1754-1765.
[45] C. Hesse, F. Goetz-Neunhoeffer, J. Neubauer, M. Braeu, P. Gaeberlein, Quantitative in situ X-ray diffraction analysis of early hydration of Portland cement at defined temperatures, Powder Diffr. 24 (2009) 112-115.
[46] B. Lothenbach, F. Winnefeld, Thermodynamic modelling of the hydration of Portland cement, Cem. Concr. Res. 36 (2006) 209-226.
[47] A. Quennoz, K.L. Scrivener, Interactions between alite and C_3A-gypsum hydrations in model cements, Cem. Concr. Res. 44 (2013) 46-54.
[48] H.F. Taylor, Cement chemistry, Thomas Telford London, 1997.
[49] D. Min, T. Mingshu, Formation and expansion of ettringite crystals, Cem. Concr. Res. 24 (1994) 119-126.
[50] H. Zheng, J. Lu, P. Shen, L. Sun, C.S. Poon, W. Li, Corrosion behavior of carbon steel in chloride-contaminated ultra-high-performance cement pastes, Cem. Concr. Compos. 128 (2022) 104443.
[51] E. Bernard, W.J. Zucha, B. Lothenbach, U. Mäder, Stability of hydrotalcite (Mg-Al layered double hydroxide) in presence of different anions, Cem. Concr. Res. 152 (2022) 106674.
[52] B. Lothenbach, D.A. Kulik, T. Matschei, M. Balonis, L. Baquerizo, B. Dilnesa, G.D. Miron, R.J. Myers, Cemdata18: A chemical thermodynamic database for hydrated Portland cements and alkali-activated materials, Cem. Concr. Res. 115 (2019) 472-506.
[53] K. Scrivener, R. Snellings, B. Lothenbach, A practical guide to microstructural analysis of cementitious materials, Crc Press, (2018) 198-200.
[54] C. Kuenzel, F. Zhang, V. Ferrandiz-Mas, C. Cheeseman, E. Gartner, The mechanism of hydration of MgO-hydromagnesite blends, Cem. Concr. Res. 103 (2018) 123-129.
[55] R.L. Frost, J.T. Kloprogge, Infrared emission spectroscopic study of brucite, Spectrochim. Acta A: Mol. Biomol. Spectrosc. 55 (1999) 2195-2205.
[56] N.C. Collier, Transition and decomposition temperatures of cement phases–a collection of thermal analysis data, Ceram-Silikaty, 60 (2016).

[57] P. Meredith, A. Donald, N. Meller, C. Hall, Tricalcium aluminate hydration: Microstructural observations by in-situ electron microscopy, J. Mater. Sci. 39 (2004) 997-1005.
[58] J.W. Bullard, E. Enjolras, W.L. George, S.G. Satterfield, J.E.J.M. Terrill, A parallel reaction-transport model applied to cement hydration and microstructure development, Model. Simul. Mater. Sci. Eng. Fail. Anal. 18 (2010) 025007.
[59] P.K. Mehta, Mechanism of sulfate attack on portland cement concrete—Another look, Cem. Concr. Res. 13 (1983) 401-406.
[60] P.K. Mehta, Effect of lime on hydration of pastes containing gypsum and calcium aluminates or calcium sulfoaluminate, J. Am. Ceram. Soc. 56 (1973) 315-319.
[61] M. Collepardi, G. Baldini, M. Pauri, M. Corradi, Tricalcium aluminate hydration in the presence of lime, gypsum or sodium sulfate, Cem. Concr. Res. 8 (1978) 571-580.
[62] H. Hirao, K. Yamada, H. Takahashi, H. Zibara, Chloride binding of cement estimated by binding isotherms of hydrates, J. Adv. Concr. Technol. 3 (2005) 77-84.
[63] M. Bukhtiyarova, A review on effect of synthesis conditions on the formation of layered double hydroxides, J. Solid State Chem. 269 (2019) 494-506.
[64] A. Seron, F. Delorme, Synthesis of layered double hydroxides (LDHs) with varying pH: A valuable contribution to the study of Mg/Al LDH formation mechanism, J. Phys. Chem. Solids, 69 (2008) 1088-1090.
[65] L.E. Lanyon, W.R. Heald, Magnesium, calcium, strontium, and barium, Meth. Soil Anal.: Part 2 Chem. Microbiol. Prop. 9 (1983) 247-262.
[66] R.D. Shannon, Revised effective ionic radii and systematic studies of interatomic distances in halides and chalcogenides, Acta Crystallogr. A 32 (1976) 751-767.
[67] Y. Wu, P. Duan, C. Yan, Role of layered double hydroxides in setting, hydration degree, microstructure and compressive strength of cement paste, Appl. Clay Sci. 158 (2018) 123-131.
[68] S. Xu, Z. Chen, B. Zhang, J. Yu, F. Zhang, D.G. Evans, Facile preparation of pure CaAl-layered double hydroxides and their application as a hardening accelerator in concrete, Chem. Eng. J. 155 (2009) 881-885.
[69] H. Li, C. Xu, X. Guan, H. Zhang, Effect of synthesis conditions and post-synthetic treatments of LiAl-LDH on the performance of sulfoaluminate cement, Adv. Cem. Res. 32 (2020) 288-295.
[70] H.-M. Ludwig, W. Zhang, Research review of cement clinker chemistry, Cem. Concr. Res. 78 (2015) 24-37.
[71] X. Liu, P. Feng, X. Yu, X. Shen, G. Geng, B. Lothenbach, The physiochemical alterations of calcium silicate hydrate (CSH) under magnesium attack, Cem. Concr. Res. 160 (2022) 106901.
[72] Y. Tao, W. Zhang, N. Li, F. Wang, S. Hu, Atomic occupancy mechanism in brownmillerite Ca_2FeAlO_5 from a thermodynamic perspective, J. Am. Ceram. Soc. 103 (2020) 635-644.
[73] M. Vandamme, F.-J. Ulm, P. Fonollosa, Nanogranular packing of C–S–H at substochiometric conditions, Cem. Concr. Res. 40 (2010) 14-26.

[74] H. Terraschke, C. Wickleder, UV, blue, green, yellow, red, and small: newest developments on Eu^{2+}-doped nanophosphors, Chem. Rev. 115 (2015) 11352-11378.
[75] K. De Weerdt, H. Justnes, M.R. Geiker, Changes in the phase assemblage of concrete exposed to sea water, Cem. Concr. Compos. 47 (2014) 53-63.
[76] K. De Weerdt, H. Justnes, The effect of sea water on the phase assemblage of hydrated cement paste, Cem. Concr. Compos. 55 (2015) 215-222.